Cell

Cytoplasmic division cycles without the nucleus and mitotic CDK/cyclin complexes

Graphical abstract

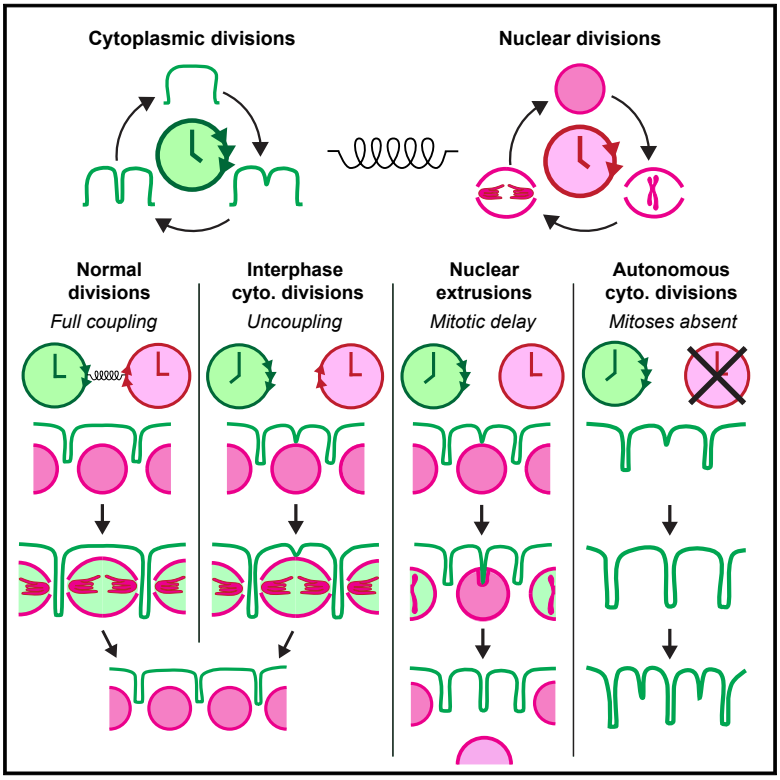

Authors

Anand Bakshi, Fabio Echegaray Iturra, Andrew Alamban, Miquel Rosas-Salvans, Sophie Dumont, Mustafa G. Aydogan

Correspondence

mustafa.aydogan@ucsf.edu

In brief

Bakshi et al. uncover during embryonic cleavage cycles in *Drosophila* that the cytoplasm can divide independently of both nuclei and the principal CDK/cyclin cell-cycle oscillator. Evidence suggests that such autonomous cytoplasmic divisions may help facilitate extrusion of mitotically delayed nuclei from the blastoderm before the onset of morphogenesis.

Highlights

- Cytoplasm can divide autonomously without the nucleus and CDK/cyclin complexes
- Cdk1 slows an otherwise faster cytoplasmic division cycle to couple it with mitosis
- Cytoplasm can use distinct microtubule organizers to transmit its division cue(s)
- Autonomous divisions help extrude mitotically delayed nuclei from the blastoderm

Bakshi et al., 2023, Cell *186*, 4694–4709
October 12, 2023
https://doi.org/10.1016/j.cell.2023.09.010

CellPress

CellPress
OPEN ACCESS

Cell

Article

Cytoplasmic division cycles without the nucleus and mitotic CDK/cyclin complexes

Anand Bakshi,[1,5] Fabio Echegaray Iturra,[1,5] Andrew Alamban,[1,2,5] Miquel Rosas-Salvans,[3] Sophie Dumont,[1,4] and Mustafa G. Aydogan[1,2,6,*]

[1]Department of Biochemistry and Biophysics, University of California, San Francisco, San Francisco, CA 94158, USA
[2]Biophysics Graduate Program, University of California, San Francisco, San Francisco, CA 94158, USA
[3]Department of Bioengineering and Therapeutic Science, University of California, San Francisco, San Francisco, CA 94158, USA
[4]Chan Zuckerberg Biohub, San Francisco, CA 94158, USA
[5]These authors contributed equally
[6]Lead contact
*Correspondence: mustafa.aydogan@ucsf.edu
https://doi.org/10.1016/j.cell.2023.09.010

SUMMARY

Cytoplasmic divisions are thought to rely on nuclear divisions and mitotic signals. We demonstrate in *Drosophila* embryos that cytoplasm can divide repeatedly without nuclei and mitotic CDK/cyclin complexes. Cdk1 normally slows an otherwise faster cytoplasmic division cycle, coupling it with nuclear divisions, and when uncoupled, cytoplasm starts dividing before mitosis. In developing embryos where CDK/cyclin activity can license mitotic microtubule (MT) organizers like the spindle, cytoplasmic divisions can occur without the centrosome, a principal organizer of interphase MTs. However, centrosomes become essential in the absence of CDK/cyclin activity, implying that the cytoplasm can employ either the centrosome-based interphase or CDK/cyclin-dependent mitotic MTs to facilitate its divisions. Finally, we present evidence that autonomous cytoplasmic divisions occur during unperturbed fly embryogenesis and that they may help extrude mitotically stalled nuclei during blastoderm formation. We postulate that cytoplasmic divisions occur in cycles governed by a yet-to-be-uncovered clock mechanism autonomous from CDK/cyclin complexes.

INTRODUCTION

The cell cycle is a series of events that leads to mitosis, such as centrosome duplication, genome replication, chromosome condensation, and spindle formation, followed by cytokinesis.[1] Prevailing models suggest that the rising levels of cyclin-dependent kinase 1 (Cdk1) activity[2,3] and/or affinity for substrates[4,5] triggers these events. Recent work, however, has demonstrated that some cell-cycle events can happen independently of Cdk1 activity.[6,7] For instance, centrioles can duplicate autonomously when the cell cycle halts, both by perturbations in dividing cells[8–10] and naturally in non-dividing cells.[11,12] Furthermore, DNA replication can continue without cell divisions,[13] and conversely, cells can divide even when DNA replication is inhibited.[14–16] Strikingly, cell divisions without DNA replication can occur even under physiological conditions, e.g., during zebrafish skin expansion[17] and meiosis.[18]

Cytoplasmic divisions have been conceptualized as a sequel to nuclear divisions.[19,20] This is the case even for cells that divide without DNA replication, as their nuclei still divide despite a decrease in hereditary material.[14–17] The signal that triggers cytoplasmic divisions is believed to be the mitotic regulation of cell-cycle kinases and spindle formation, as they are thought to spatiotemporally control cleavage furrowing.[19,20] To what extent they are required for cytoplasmic divisions, however, remains unclear. Here, we show in *Drosophila* embryos that the cytoplasm can compartmentalize, mature its cortex, and divide repeatedly without nuclei, and they can do this independent of mitotic CDK/cyclin complexes. We find that Cdk1 normally slows an otherwise faster cytoplasmic division cycle to couple it with nuclear divisions. When the two uncouple, the cytoplasm begins to divide in interphase before mitotic entry and spindle formation. Remarkably, we find that autonomous cytoplasmic divisions also occur during unperturbed embryogenesis. Our evidence suggests that this may confer a physiological advantage by enabling the extrusion of mitotically delayed nuclei from the blastoderm, thereby preserving genome integrity at the onset of morphogenesis.

RESULTS

Cytoplasm can start its division before mitotic entry and divide without a nucleus in fly embryos

Cell cycles in *Drosophila* embryos are a valuable system to investigate the trigger of cytoplasmic divisions, as one could follow them synchronously in the blastoderm[21,22] (Video S1). Cortical furrowing in these embryos begins at prophase during cycles 11–13, and once the embryos exit these cycles, the

cleavage furrows initiate again and continue through a prolonged cycle 14 before morphogenesis.[23] Despite reports that some nuclear and cytoplasmic events can occur irrespective of each other during fly development,[9,24,25] the prevailing dogma is that nuclear and cytoplasmic divisions are temporally coupled to occur in a coordinated manner.[26,27] In embryos expressing His2(Av)-(m)RFP (nuclei) and MRLC-GFP (myosin regulatory light chain), we confirmed that this is generally the case (Figure S1A). In some cases, however, we observed an intriguing mismatch between the number of nuclei in the field of view and the associated cytoplasmic compartments (Figures 1A–1D).

A significant fraction of the cytoplasmic compartments (Figure 1E) started dividing equatorially before mitotic entry (Figure 1F) in the blastoderm (Figures 1A and 1B). These early divisions occurred in mid-S-phase prior to nuclear envelope breakdown (NEB) (Figure 1A, bottom; Video S1). These properties are distinct from the previously identified Rho-A-induced, equatorial cleavage furrows, which form over the central spindle during metaphase-to-anaphase transition in fly embryos.[24] To determine whether the observed cytokinetic ring-like myosin bridges (Figure 1A) were accompanied by other cleavage furrow components, we generated flies expressing His2-RFP and Moe-(ABD-)GFP, labeling the actin-binding domain (ABD) of Moesin. Like MRLC-GFP, Moe-GFP decorated the early division rings (Figures 1C and S1B). The divisions were also accompanied by plasma membrane ingression, observed in embryos expressing Toll-Venus (a plasma membrane protein) and His2-RFP (Figures 1D and S1C). These divisions are unlikely to be fortuitous events, as they happened synchronously in mid-to-late interphase and across the whole field of view (Figures S2A and S2B). The daughters of early and regularly dividing compartments did not differ significantly in size, implying that the timing of cleavage furrowing does not impact cytoplasmic division fidelity (Figure 1G). These suggested that the early cytoplasmic divisions in fly embryos display features of normal cell divisions but can occur synchronously prior to mitotic entry and nuclear division.

A closer examination also revealed a rare fraction of cytoplasmic compartments that, by contrast, were void of nuclei (Figures 1E and 2A–2C). Remarkably, these cytoplasmic compartments appeared intact and capable of several rounds of cytoplasmic divisions (Figures 2A–2C; Video S2). Despite lacking nuclei, these compartments contained organelles, e.g., the endoplasmic reticulum (ER) (Figure S2D) and mitochondria (Figure S2E), which segregated as they normally would in regular divisions (Figures S2F and S2G). These results suggested that the cytoplasmic divisions could occur without a nucleus in fly embryos.

Cytoplasmic division cycles can run without nuclei independently of the mitotic CDK/cyclin complexes

CDK/cyclin complex is recognized as the master clock of the cell cycle.[18,28] If the cytoplasmic divisions that occur in interphase (Figures 1A–1D) were regulated by the CDK system, then their timing would change upon modulating Cdk1 activity. To test this, we examined the timing of these early divisions in $Cdc25^{+/-}$ and $Chk1^{-/-}$ conditions, which decreases[29] or increases[30] Cdk1 activity, respectively. As expected, the interphase length was markedly different between the two mutant conditions (Figure 1H). Yet, the interphase cytoplasmic divisions occurred with comparable temporal dynamics (Figure 1I), suggesting that they are uncoupled from the CDK/cyclin system.

To directly test whether mitotic CDK/cyclin complexes regulate cytoplasmic divisions, we injected a double-stranded RNA (dsRNA) cocktail targeting all mitotic cyclins (A, B, and B3)[9,10,31] into embryos expressing MRLC-GFP soon after their fertilization (~cycle 2–4). As centriole duplications can occur independently of nuclear cycles,[9,10] we simultaneously expressed Sas-6-mCherry to monitor the cortical blastoderm. We found that the cytoplasm can compartmentalize even in the absence of any blastoderm nuclei in these early arrested embryos (Figure 3A; see Figures S3A–S3C for controls). Like in a regular blastoderm, cytoplasmic compartments in arrested embryos also became ensheathed with plasma membrane (Figure 3A, middle row). Furthermore, centrioles had matured into centrosomes, evident from their microtubule (MT) nucleation (Figure 3A, bottom), suggesting that these compartments show architectural similarities to their counterparts in unperturbed embryos. Remarkably, the cytoplasm in arrested embryos divided repeatedly as centrosomes separated, generating lineages of cytoplasmic compartments without any blastoderm nuclei (Figure 3B; Video S3). Note an example lineage going through 4 rounds of divisions, first to generate *P*, then from *P* to *B*, then to B_a and B_b, and then to their daughters (Figure 3B). As a control, we generated flies that express MRLC-mCherry simultaneously with an established Förster resonance energy transfer (FRET) biosensor that reports the oscillatory activity of Cdk1 during the cell cycle[31,32] (Figure 3C). As with previous reports,[31,32] we observed oscillations in Cdk1 activity that are concurrent with the cell cycles in developing embryos (Figures 3D and 3F). Conversely, there were no Cdk1 activity oscillations associated with autonomous cytoplasmic divisions in arrested embryos (Figures 3E and 3F), demonstrating CDK/cyclin complexes are indeed halted in these experiments.

The division-to-division durations of autonomous cytoplasmic divisions are normally distributed, suggesting that these cycles occur with a distinct period in each generation (Figure 3G). Interestingly, just like the nuclear cycles in regular embryos, autonomous cytoplasmic divisions also ran gradually slower as the maternal deposits were consumed (Figure 3G). Nonetheless, we found that the cytoplasmic division cycles are 1.6–2.3× faster on average than a nuclear division cycle at corresponding blastoderm stages (judged by the absolute time spent post-fertilization) (Figure 3H). Next, we compared the autonomous division period with when the early divisions occur in interphase at the reciprocal blastoderm stage (i.e., cycle 12). We found the two durations to be essentially the same (Figure 3I). As such, when the cytoplasmic divisions uncouple from nuclear cycles in regular embryos (Figures 1H and 1I), they occur at a pace similar to that of the autonomous divisions in arrested embryos (Figure 3I). These results suggest that mitotic CDK/cyclins normally slow an otherwise faster cytoplasmic division cycle to couple it with nuclear divisions. When uncoupled, the cytoplasm starts its division before mitosis (Figures 1A and 1B).

To test whether cytoplasmic divisions require *de novo* protein synthesis when uncoupled from nuclear divisions, we assessed the impact of cycloheximide (CHX), a translation inhibitor (Figures 2D and 2E), whose injection did not perturb the size of

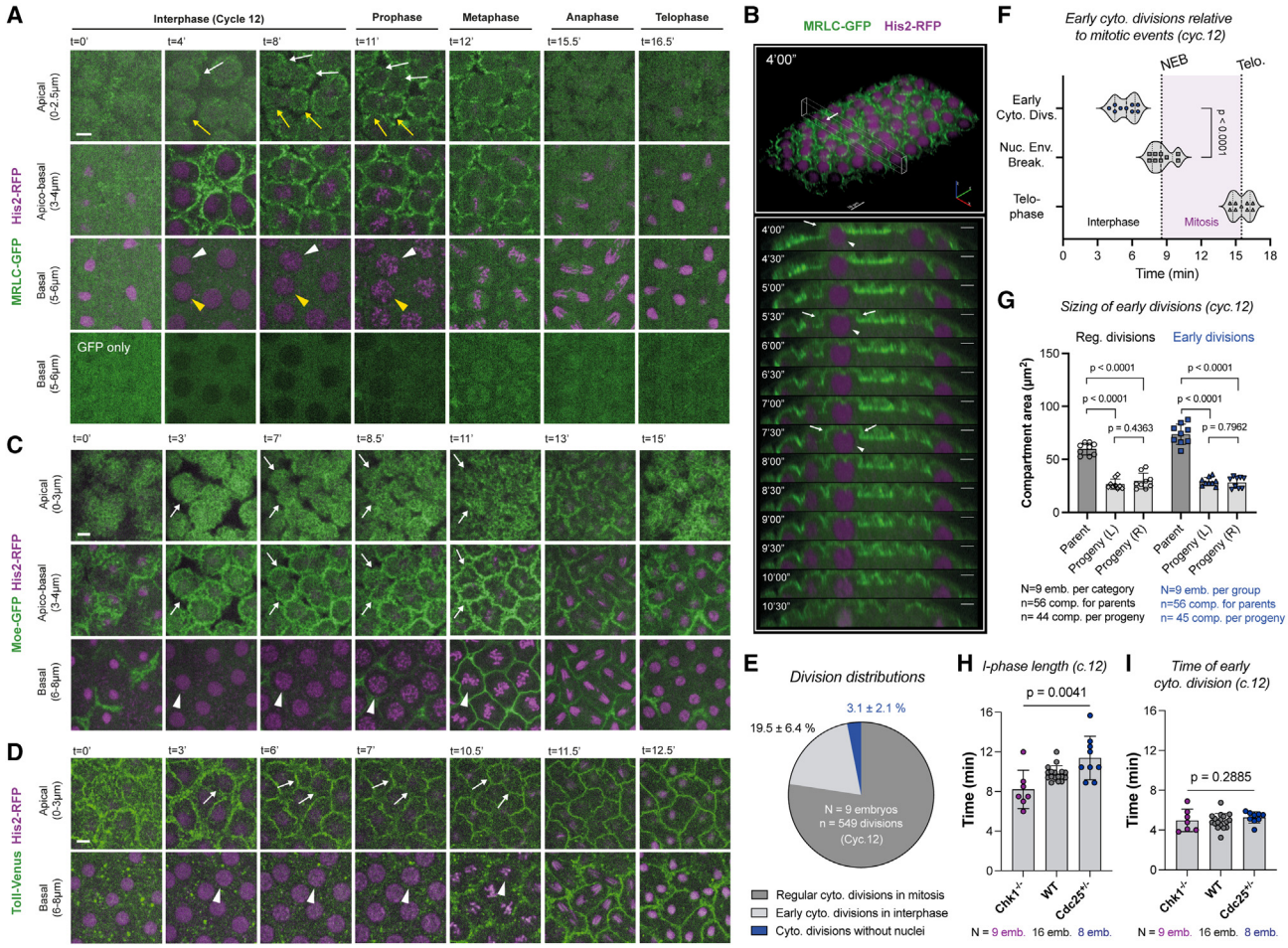

Figure 1. Cytoplasmic divisions can uncouple from nuclear divisions to start in mid-interphase in fly embryos

(A–D) Cycle 12 embryos expressing His2-RFP simultaneously with (A and B) MRLC-GFP, (C) Moe-GFP, or (D) Toll-Venus. In (A), (C), and (D), apical panels visualize the cytoplasmic compartments. Basal panels depict the nuclei. A fraction of cytoplasmic compartments (19.5% ± 6.4%) start dividing in interphase (A–D; white and/or yellow arrows). Nuclei that correspond to these divisions (with color-matching arrowheads) are still in interphase (the basal row). (B) provides an x-z kymograph of the early dividing compartment highlighted with white arrows in (A). Nuclear envelope breakdown (NEB) is judged by the entry of MRLC-GFP into the nucleoplasm, as illustrated in the bottom row of (A). Scale bars, 5 µm.

(E) Pie chart for various types of cytoplasmic divisions, where cytoplasmic divisions without nuclei (Figures 2A–2C) are also accounted for.

(F) Violin plots show the time of early cytoplasmic division events in relation to NEB and telophase (n = 9 embryos).

(G) Bar graphs demonstrate cytoplasmic compartment size at its maximum at NEB in comparison with their daughters (at the beginning of next interphase).

(H and I) Bar graphs show that (H) despite a significant change in interphase length induced by Chk1$^{-/-}$ and Cdc25$^{+/-}$, (I) the time of early cytoplasmic divisions remains unchanged.

All analyses (E)–(I) were performed in cycle 12 embryos expressing MRLC-GFP and His2-RFP. Statistical significance of the time gradients in (H) and (I) was assessed using a Kruskal-Wallis test. Statistical significance on all other panels was assessed using a Welch's t test (for Gaussian distributed data) or a Mann-Whitney test. Each data point in (F) represents an embryo, whose distributions are indicated with quartile lines and a probability density estimation using the kernel plot. Data in (G)–(I) are represented by mean ± SD where each data point represents the average from one embryo.

See also Figures S1 and S2.

cytoplasmic compartments in an adverse way (Figure 2E; see vehicle controls in Figures S3D and S3E). As expected, although the control embryos progressed through their cycles normally (Figures S3D and S3F), the CHX-injected ones were arrested in interphase—evident from the lack of NEB (Figure 2D, bottom). Despite this global translation shutdown and the arrest in nuclear cycle progression, ~60% of cytoplasmic compartments appeared to continue their divisions and did so for at least two additional rounds for ~50% of the time (Figures 2D and 2F; see how a compartment labeled *A* generates 4 daughter compartments after 2 rounds of division). Importantly, like the early interphase divisions (Figures 1G and S2B), cytoplasmic divisions in CHX-injected embryos appeared to occur symmetrically and synchronously throughout the embryo (Figures 2G and S2C). These findings suggest that cytoplasmic division cycles might be regulated by a post-translational mechanism, unlike CDK/cyclin complexes that require cyclin re-synthesis at every nuclear cycle.[33]

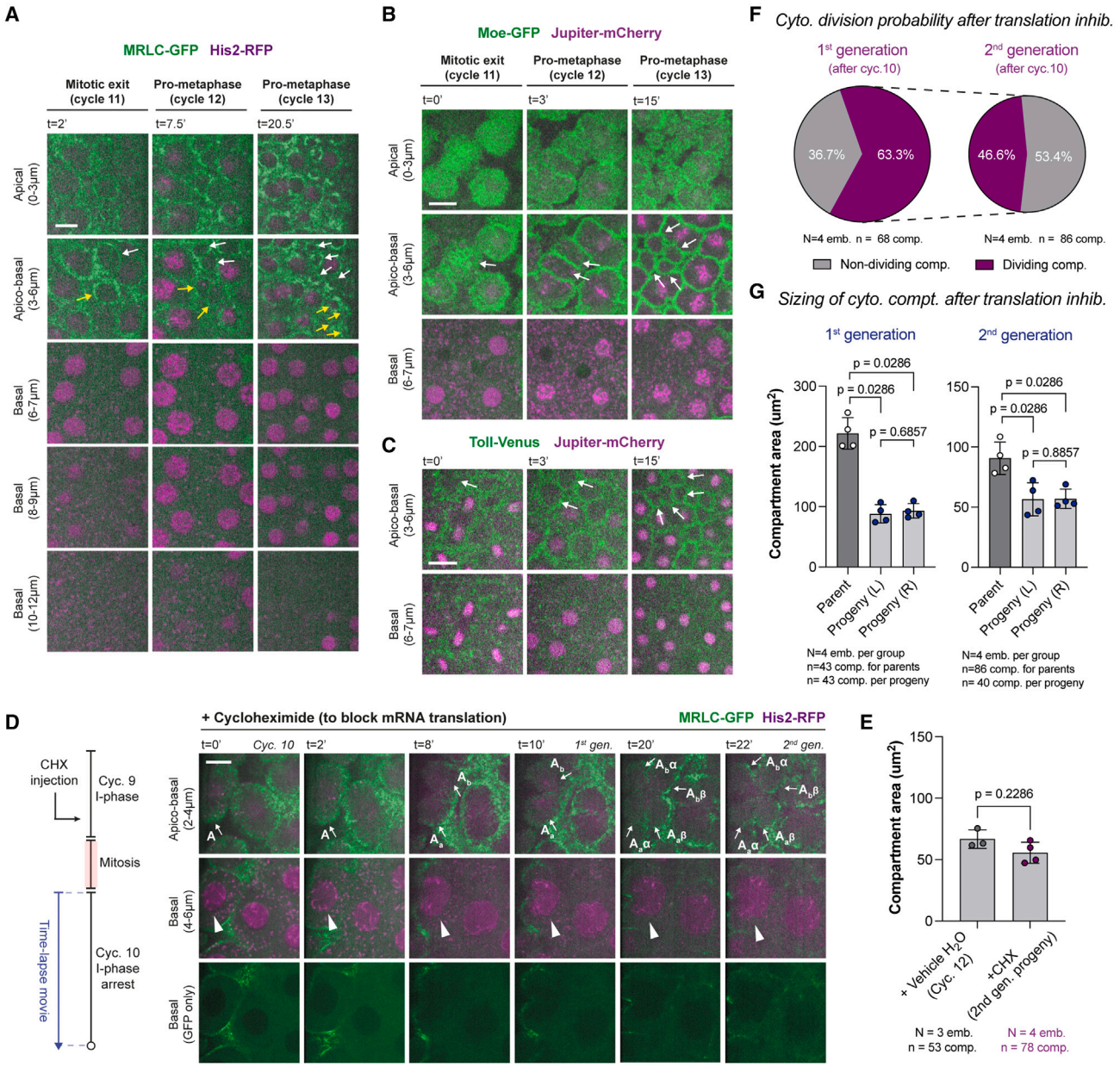

Figure 2. Cytoplasmic division cycles can occur without the nucleus or mRNA translation

(A–C) Micrographs depict a rare fraction of cytoplasmic compartments (3.1% ± 2.1%) that can divide without nuclei (white and/or yellow arrows). A deeper image series is provided in (A) to demonstrate that there are no lurking nuclei.

(D) Translation inhibition by cycloheximide (CHX) does not prevent further cytoplasmic divisions (apico-basal), despite an arrest of nuclear cycle 10 (basal). Arrows and arrowheads highlight the dividing compartments and arrested nuclei, respectively. Images are a representative set from 4 embryos injected with the drug.

(E) Bar graphs for cytoplasmic compartment size under vehicle (H_2O) or CHX conditions.

(F) Pie charts for the proportion of cytoplasmic compartments that can continue their divisions in the first and second generation after CHX injection.

(G) Bar graphs for maximum compartment sizes under CHX condition, in comparison with their daughter compartment sizes at the beginning of the next cycle. Analyses and experiments (E)–(G) were performed in embryos expressing MRLC-GFP and His2-RFP. Data (E) and (G) are represented mean ± SD, where each data point represents the average from each embryo. Statistical significance was assessed using a Welch's t test (for Gaussian distributed data) or a Mann-Whitney test. Scale bars, 10 µm.

See also Figures S2 and S3.

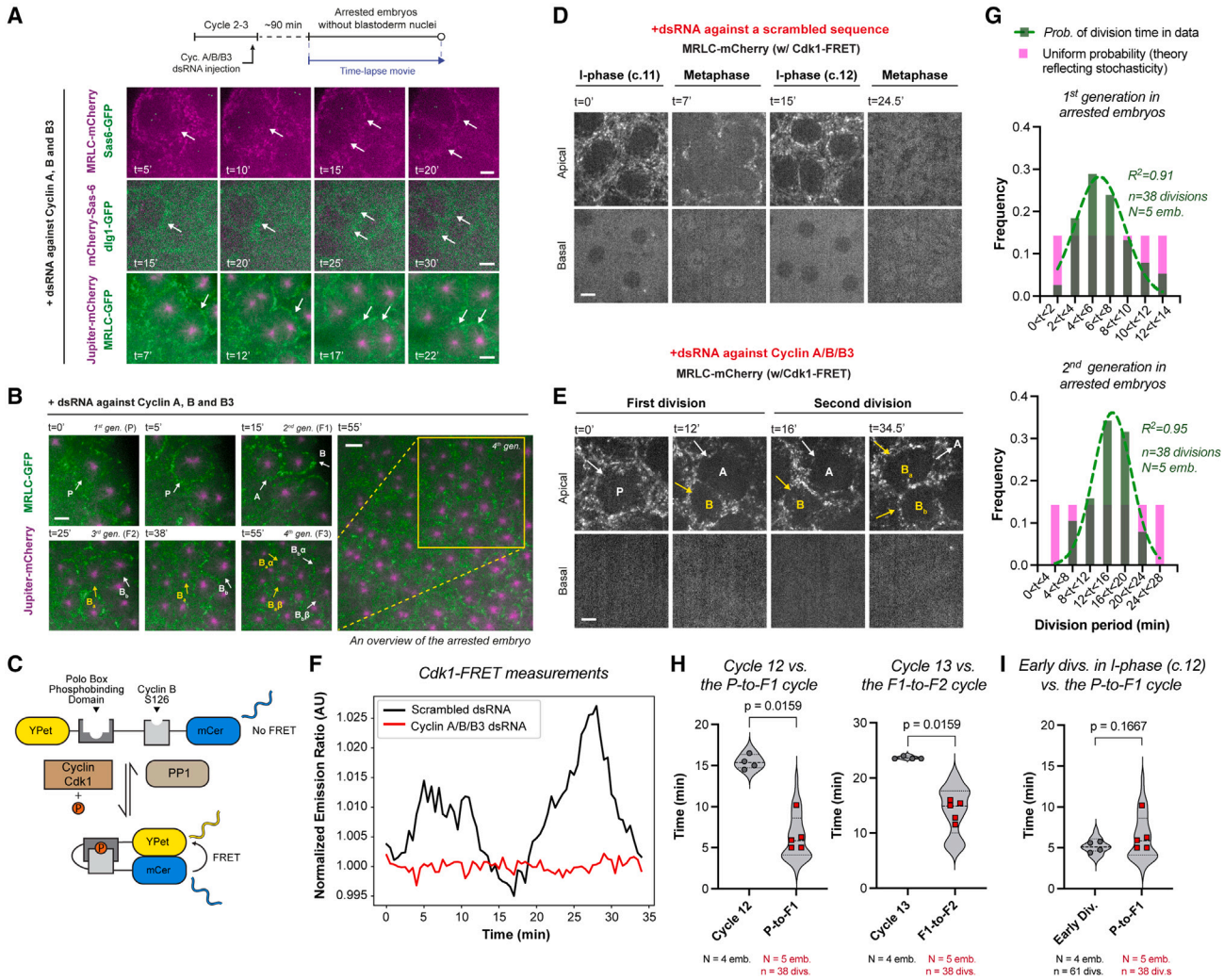

Figure 3. Cytoplasmic divisions can occur periodically without the nucleus and mitotic CDK/cyclin complexes, and they can do so faster than nuclear divisions

(A) Cyclin A-B-B3 triple cocktail dsRNA injection in embryos that express (top) MRLC-mCherry and Sas-6-GFP; (middle) mCherry-Sas-6 and dlg1-GFP (plasma membrane); (bottom) MRLC-GFP and Jupiter-mCherry (n = 9 embryos). Illustrated by white arrows, see the formation and division of compartments without nuclei—judged by the complete lack of nuclear shadows basally, as successfully done before using the nuclear retention of otherwise cytoplasmic proteins[10] (see Figure S3A for validations).

(B) Cytoplasmic divisions continue in arrested embryos, yielding multiple generations (see for example, *P* to *B*, then to B_a and B_b, then to $B_a\alpha$, $B_a\beta$, $B_b\alpha$, and $B_b\beta$).

(C) Cartoon diagram for an established Cdk1/Protein Phosphatase 1 (PP1) FRET biosensor[31,32] (see STAR Methods).

(D) Micrographs illustrate cell cycles in regular embryos expressing Cdk1-FRET and MRLC-mCherry, injected with a scrambled dsRNA sequence.

(E) Autonomous cytoplasmic divisions in embryos expressing the same markers as in (D) but with cyclin A/B/B3 dsRNAs.

(F) Cdk1/PP1 FRET dynamics were quantified directly from time-lapse videos depicted in (D) and (E) (see STAR Methods), representative from n = 3 embryos in each condition.

(G) Graphs show the period distributions in the first and second generations of cytoplasmic divisions in arrested embryos (green bars), after the initial emergence of cytoplasmic compartments. The data are distributed normally with a defined center, as opposed to a uniform distribution (theoretical pink bars) that implicates stochasticity. R^2 values indicate the goodness of Gaussian fit in green.

(H) Violin plots compare autonomous cytoplasmic division period (red data points) with the period of nuclear divisions at corresponding blastoderm stages in control embryos (gray data points).

(I) Violin plot compares autonomous cytoplasmic division period (red data points) with the time of early cytoplasmic divisions in the interphase of scrambled dsRNA embryos (gray data points).

Analyses (G)–(I) were performed on embryos expressing MRLC-GFP and Jupiter-mCherry under indicated conditions. Each data point (H) and (I) represents an embryo (N), whose distributions are indicated with quartile lines derived from the underlying cytoplasmic division data (n) and a probability density estimation using the kernel plot. Statistical significance was assessed using a Welch's t test (for Gaussian distributed data) or a Mann-Whitney test. Scale bars, 5 μm. See also Figure S3.

Together, our results demonstrate that the cytoplasm can compartmentalize and partition without nuclei and can sustain periodic divisions autonomously of mitotic CDK/cyclin complexes even under anuclear conditions.

The cytoplasmic division cycle can occur without centrosomes in developing embryos

A number of MT organizers have been demonstrated to help transmit the cytoplasmic division cues during the cell cycle,[34,35] including the interphase centrosomes,[36,37] the mitotic spindles, and the central spindles deployed in late anaphase.[38–40] We observed that centrioles were present during interphase divisions (Figure S4A), during the divisions without nuclei (Figure S4B), as well as during the autonomous divisions in arrested embryos (Figure 3A). Combined with the findings that centrosome duplications can occur independently of nuclear divisions,[8–10] these suggested that centrosomes might regulate the cytoplasmic division cycle. To test, we generated flies expressing MRLC-mCherry and Sas-6-GFP, and attempted to laser ablate centrioles in early/mid-interphase, when mother centrioles grow their daughters[41,42] (see ablation controls in Figures S5A and S5B; STAR Methods).

Upon ablations, we observed that the cytoplasmic compartments remained intact (Figure 4A) and maintained roughly similar sizes in comparison with their unablated neighbors (Figure 4B). Remarkably, cytoplasmic compartments continued their divisions at least for another round despite lacking centrioles (Figure 4A; in all 5 of our successful ablation experiments) and yielded daughter compartments of similar sizes (Figure 4B). Repeating the same experiments but in embryos that express Sas-6-GFP and Jupiter-mCherry (MTs), we found that centriole ablation abolishes centrosomal MT organization (Figure 4C), evident from both the disassembly of their MTs in interphase (Figure 4D; see t = 0″–105″) and the absence of centrosomal MTs in mitosis (Figure 4D; t = 225″–345″). To control that our ablations are specific to centrosomes and not some other parts of the cytoplasm, we ablated two regions directly neighboring the centriole pair but not on them (Figure S5C). This perturbation neither ablated the neighboring centrioles, nor influenced the division cycle in any adverse way. These indicate that centrosomes and their astral MTs are not necessary to transmit the cytoplasmic division signal in developing embryos.

Although centrosomes appeared dispensable for cytoplasmic divisions in cycling embryos, they might be required for the initial formation of cytoplasmic compartments, which can organize and divide autonomously in the absence of nuclei and mitotic MT organizers (Figure 3). To test this possibility, we used unfertilized eggs, which—unlike the cycling embryos—do not form cytoplasmic compartments by default (Figure S4C). These eggs can be induced to trigger *de novo* centriole biogenesis by over-expressing Polo-like kinase 4 (Plk4),[43,44] so we examined whether this can drive the formation of cytoplasmic compartments. We found that *de novo* centrioles, despite nucleating MTs (Figures 4E and S4D), do not trigger cytoplasmic compartment formation (Figures 4E and S4E). As high Cdk1 activity is refractory for myosin localization,[45] it may prevent the formation of cytoplasmic compartments even when centrosomes are present. To test, we examined the effect of Roscovitine (inhibiting Cdk1 activity[46]) in unfertilized eggs with *de novo* centrioles. Even when injected with Roscovitine, these eggs did not display any cytoplasmic compartments (Figures 4E and S4F). Together, these results suggest that centrosomes are not sufficient to trigger cytoplasmic divisions in developing fly embryos.

The cytoplasmic cycle can employ distinct MT organizers to transmit its division cues

Although centrosomes are major organizers of MT polymerization for cytoplasmic divisions,[47–49] cells could employ other MT organizers (above) to help transmit the division cues.[50] Indeed, a global inhibition of MT polymerization by colchicine completely abolishes cytoplasmic compartments and their divisions in cycling embryos (Figures 5A and S6A–S6D), demonstrating the necessity of mitotic MTs as the centrosomes are dispensable (Figure 4A). Together, these observations suggest that alternative MT organizers could be deployed in mitosis to mediate cytoplasmic divisions without centrosomes and their astral MTs.

As in vertebrate tissues,[51,52] astral and chromatin-mediated MT polymerization can act redundantly to help assemble mitotic MT organizers in fly embryos.[53,54] To test whether chromatin-mediated MTs can be sufficient to maintain cytoplasmic compartments, we administrated low-dose nocodazole to selectively depolymerize astral MTs.[55,56] As expected, although the astral MT capacity was greatly diminished, the chromatin-mediated MTs appeared intact (Figures 5A, S6E, and S6F). Despite an early mitotic arrest leading to transient myosin delocalization, the cytoplasmic compartments formed and remained largely intact (Figures 5A, S6E, and S6F), maintaining sizes comparable to those in control embryos (Figure 5B). These results help explain, at least in part, how developing embryos could assemble mitotic MT organizers and sustain cytoplasmic divisions when centrosomes are ablated (Figure 4D; t = 225″–345″).

We next tested whether the opposite holds true: do centrosomes become essential when mitotic MT organizers are not available? We tested this by ablating centrosomes in arrested embryos that remain in interphase and lack all mitotic MT organizers. Just as in developing embryos (Figure 4B), ablating centrosomes in arrested embryos did not perturb the cytoplasmic compartment size (Figure 5D). Crucially, the cytoplasmic compartments without centrosomes ceased divisions in arrested embryos (Figures 5C and 5E).

Together, these findings suggest that the cytoplasmic cycle can employ distinct MT organizers to transmit its division cues based on their availability. In developing embryos where CDK/cyclin is active and can license mitotic MT organizers (e.g., the mitotic and central spindles), cytoplasmic divisions can occur without centrosomes. By contrast, when CDK/cyclin is inactive and mitotic MT sources are unavailable, centrosomes become essential to sustain the autonomous cytoplasmic division cycle.

The cytoplasmic cycle can transmit its division cues independently of actin's myosin-based contractility in early fly embryos

Just as the MT organizers, actin's myosin-based contractility is thought to help transmit the division cues in a timely fashion.[19,57] To test this, we adopted two independent approaches to inhibit the activity of Rho-GTPase, a key upstream effector of myosin. First, we administrated purified exoenzyme C3 transferase, an

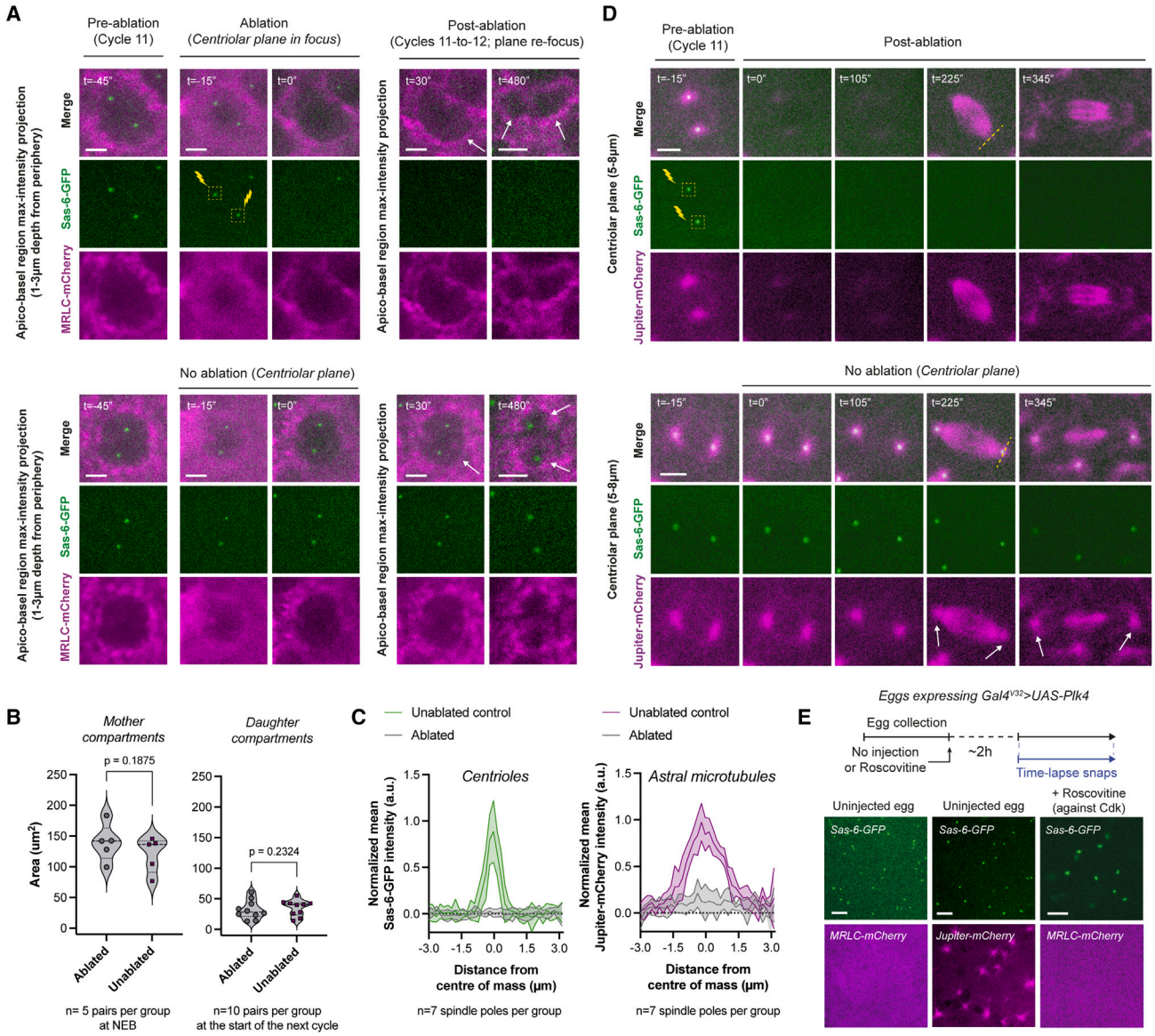

Figure 4. Centrosomes are neither necessary nor sufficient to trigger cytoplasmic divisions in developing fly embryos

(A) Micrographs depict compartments (MRLC-mCherry) where the centrioles (Sas-6-GFP) were ablated in early interphase (top) or were uninterrupted (bottom). Successful ablations (n = 5 embryos) were judged by the elimination of Sas-6-GFP and its persistent absence. See further controls on inadvertent or intentional bleaching in Figures S5A and S5B. Cytoplasmic compartments without centrioles continue to divide (top panels with white arrows).

(B) Violin plots compare cytoplasmic compartment sizes immediately after ablation in cycle 11 (left), or immediately after their divisions (cycle 12) to compare their progeny sizes (right).

(C) Radial profiles of the normalized mean Sas-6-GFP (centriole) and Jupiter-mCherry (astral MT) intensity values from mitotic spindle poles under indicated ablation conditions in (D).

(D) An experiment mimicking (A) but performed in embryos expressing Sas-6-GFP and Jupiter-mCherry (n = 4 embryos). White arrows (bottom) highlight the intact centrosomes and astral MTs. Dashed yellow lines (top) signify the regions used for radial profiles depicted in (C).

(E) Images illustrate *de novo* centriole formation in unfertilized eggs, either unperturbed (left and middle; n = 5 and 11, respectively) or +Roscovitine (n = 9). See Figures S4D–S4F for their time-lapse snapshots.

Each data point in (B) represents a single compartment (n), whose distributions are indicated with quartile lines and a probability density estimation using the kernel plot. Data in (C) are represented mean ± SD. Statistical significance was assessed using a Welch's t test (for Gaussian distributed data) or a Mann-Whitney test. Scale bars, 5 µm.

See also Figures S4 and S5.

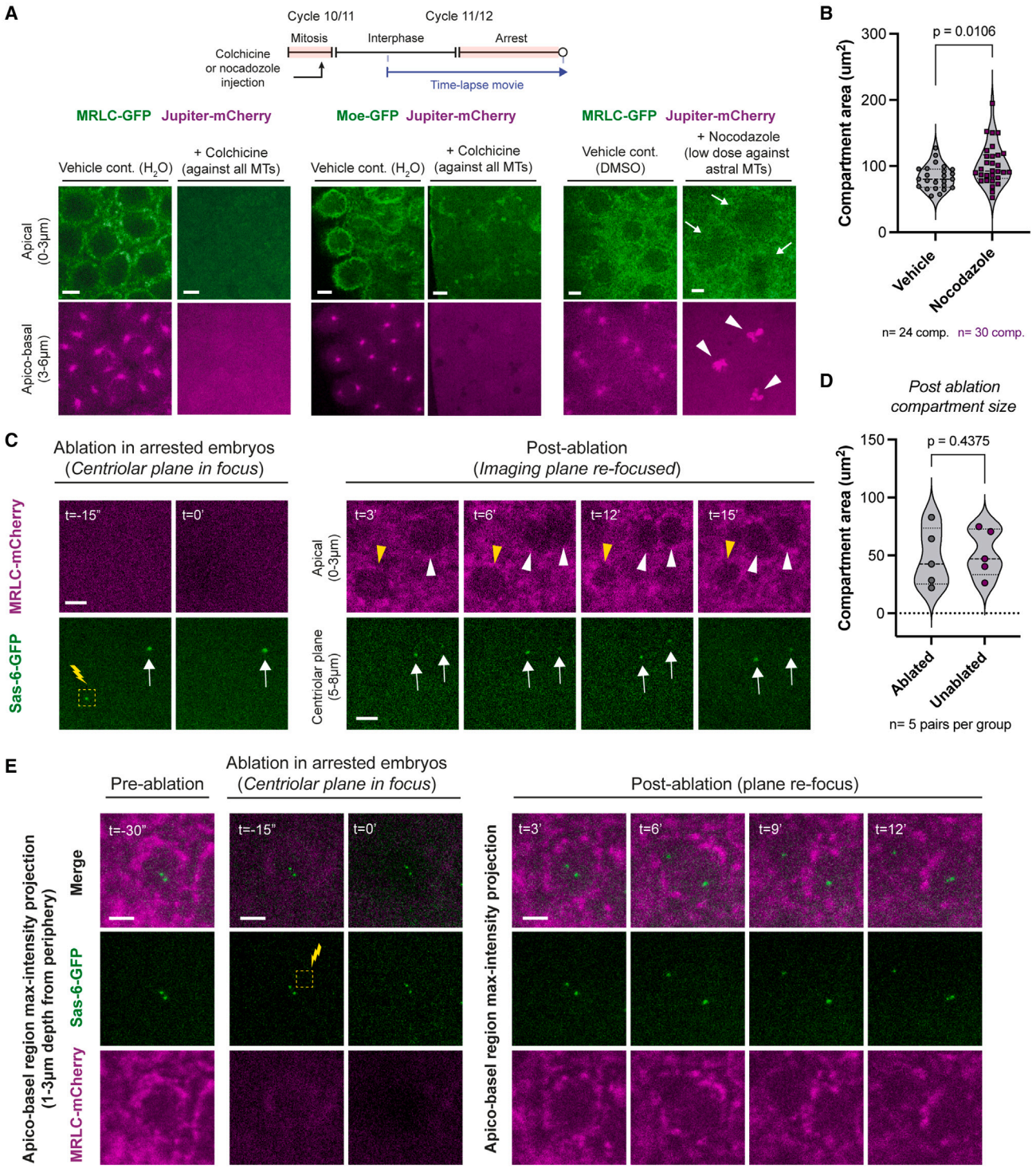

Figure 5. The cytoplasmic cycle can employ distinct MT organizers to transmit its division cues based on their availability

(A) Micrographs depict cytoplasmic compartments, or their absence, under indicated conditions. White arrows highlight how cytoplasmic compartments still form, though less robustly, when chromatin mediates MT polymerization (pointed at by white arrowheads). See Figure S6 legend for sample sizes.

(B) Violin plots compare cytoplasmic compartment size in embryos injected with nocodazole or its vehicle from (A).

(C) Laser ablation of centrioles in embryos injected with cyclin A-B-B3 dsRNA. Yellow arrowheads denote a cytoplasmic compartment where the centrioles were ablated (the first 15 min of a ~1 h capture; representative of all 5 successful ablations). White arrowheads follow an unperturbed cytoplasmic compartment. White arrows indicate the unablated centrioles. Images display a representative experiment from 5 successful independent trials.

(legend continued on next page)

ADP ribosyl transferase that inhibits RhoA/B/C, which prevents myosin II-based contractility at the onset of morphogenesis in cycle 14.[58,59] Injection of exoenzyme C3 into cycle 14 embryos confirmed that morphogenesis was indeed disrupted (Figure 6A). When injected in earlier cycles (Figures 6B and 6C), however, cytoplasmic compartments persisted (Figure 6C) and notably showed early divisions in interphase, as well as divisions without nuclei (Figure 6B). Next, we administrated Rhosin hydrochloride (inhibiting RhoA's guanine nucleotide-exhange factor binding domain) and found that this fully mimicked the former results (Figures 6A–6C). Importantly, in both exoenzyme C3 and Rhosin experiments, cortical myosin localization was impaired only at the onset of morphogenesis (Figure 6A), but not in the preceding cell cycles (Figure 6B). These results suggest that RhoA is not essential to transmit cytoplasmic division cues in early fly embryos—even when the divisions happen in interphase or without nuclei.

Downstream, myosin is regulated via the activating phosphorylations by Rho-associated protein kinase (ROCK). We therefore injected Y-27362, a selective inhibitor of ROCK, preventing myosin II-based contractility in fly embryos.[45] Although Y-27362 significantly impaired cortical myosin recruitment (Figure 6D), cytosolic MRLC-GFP signal appeared to generate subtle halo-like patches around the nuclei (Figure 6D; see bottom panels at t = 4′ and t = 6′). This hinted that the cytoplasmic compartments may still be intact. Indeed, embryos injected with Y-27362 still formed compartments that were decorated with actin and plasma membrane (Figures 6E and 6F) and displayed comparable sizes to those in control embryos (Figures 6G and 6H). However, cytoplasmic divisions in the Y-27362 embryos occurred significantly slower (Figures 6I and 6J), despite the nuclear cycle length remaining the same (Figures 6I and 6J). This delay was also manifested in the form of multiple nuclei encompassed by the same compartment at the start of interphase (Figures 6E and 6F), as well as the occasional synkaryon formation due to ill-segregated nuclei (Figure 6H, right). Nonetheless, the Y-27362 embryos retained their ability to induce cytoplasmic divisions in interphase (though expectedly rarer and mostly in longer cycles, i.e., cycle 13) and divisions without nuclei (Figure 6H, left and middle).

These results indicate that cytoplasmic compartments in early fly embryos can form and transmit their division cues independently of actin's myosin II-based contractility. Our findings suggest that myosin II-based contractility appears to serve as a structural component that facilitates the pace of cytoplasmic divisions, to maintain synchrony with nuclear divisions.

Autonomous cytoplasmic divisions may safeguard embryonic development by helping extrude mitotically delayed nuclei from the blastoderm

To explore the physiological relevance of autonomous cytoplasmic divisions, we carefully examined early cytoplasmic divisions (Figure 1) with regards to the status of nuclear divisions associated with them. We did this because we found that the mitotic entry of a small but reproducible number of nuclei was delayed by 1.5–2 min (Figures 7A and 7C, see the delay in bottom; Video S4, white arrows labeled "type 1"), yet the cytoplasmic compartments associated with them have already divided (Figure 7A, white arrows; n = 16 mitotically delayed nuclei from 9 embryos). Although only 12% of early cytoplasmic divisions presented in Figure 1 had mitotically delayed nuclei (Figure 7D), cytoplasmic compartments bisecting the delayed nuclei furrowed significantly deeper than the ones without (Figure 7E). As delayed nuclei slipped mitosis and failed to divide (Figure 7B), the cytoplasmic compartments that had divided above them appeared to contract and push the undivided nuclei basally, leading to their elimination from the blastoderm in the next cell cycle (Figure 7B).

Nuclear fallout is the spontaneous elimination of nuclei from the fly blastoderm, often observed as a consequence of DNA damages associated with spindle segregation errors, such as lagging chromosomes and/or chromosome bridges.[60–65] Indeed, we also observed that nuclei with these errors (Figure S7A) were largely eliminated from the blastoderm (Figures S7B and S7C; 26 eliminations out of 39 cases with chromosome segregation errors; Figure 7M for quantifications; Video S4). However, nuclei with chromosome segregation errors did not appear to delay the onset of mitosis nor failed their divisions (Figures S7B and S7C). Furthermore, the damaged nuclei were not accompanied by early cytoplasmic divisions that furrowed as deep as the ones associated with the delayed nuclei (Figures S7B and S7C). By contrast, the delayed nuclei did not show any damage associated with incomplete DNA replication (Figures 7A and 7B; Video S4). These results suggest that nuclear eliminations associated with chromosome segregation errors and that with mitotically delayed nuclei observed here are likely distinct processes.

As such, we postulate the possibility of a novel blastoderm quality control mechanism, in which mitotically delayed nuclei might be extruded by autonomously dividing cytoplasmic compartments. This hypothesis posits two major predictions: (1) since delayed nucleus elimination is associated with slower NEB and a nuclear division failure (Figures 7A and 7B), lowering Cdk1 activity would be predicted to trigger local mitotic delays more frequently (Figure 7F). As myosin's cortical localization is normally inhibited by high Cdk1 activity,[45] this could also explain why the cytoplasmic compartments that encapsulate mitotically delayed nuclei can divide early (Figure 7D) and furrow deeper (Figure 7E). (2) In the complete absence of cytoplasmic compartments, the delayed nuclei would no longer be extruded (Figure 7K).

To test prediction 1 (Figure 7F), we examined CycB$^{+/-}$ embryos (Figures 7G, S7D, and S7E). We found that some of the CycB$^{+/-}$ embryos displayed more local mitotic delays (Figures 7G and S7E; Video S5), accompanied by autonomous cytoplasmic divisions (Figure S7E) and followed by clusters of nuclear elimination

(D) Violin plots compare cytoplasmic compartment size immediately after ablation between the ablated and unablated groups.
(E) Same experiment as in (C), except that a region without centrioles was ablated as a control. Images display a representative example from 3 successful independent trials.
Each data point in (B) and (D) represents a single compartment, whose distributions are indicated with quartile lines and a probability density estimation using the kernel plot. Statistical significance was assessed using a Welch's t test (for Gaussian distributed data) or a Mann-Whitney test. Scale bars, 5 μm.
See also Figure S6.

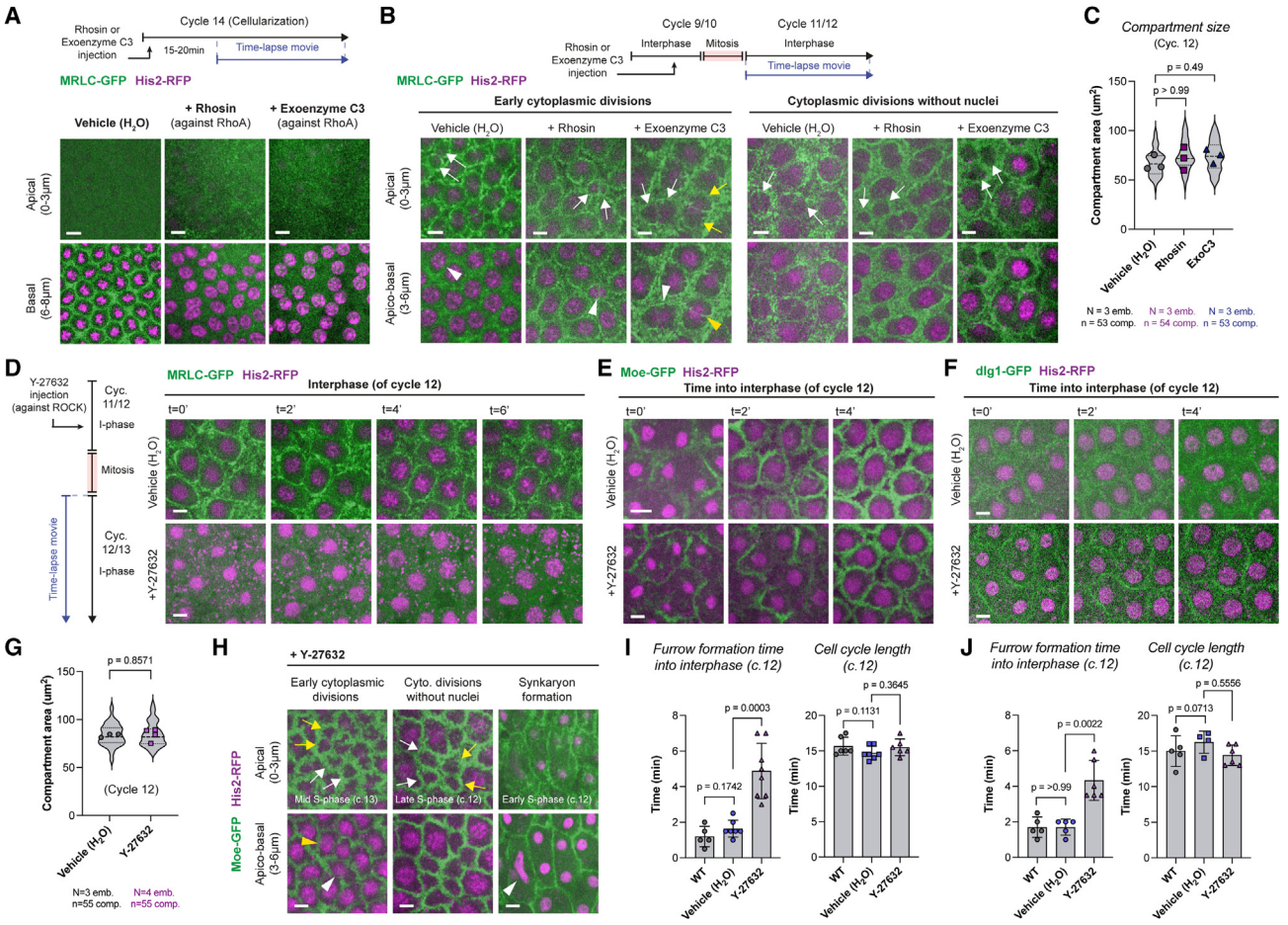

Figure 6. The cytoplasmic cycle can transmit its division cues independently of actin's myosin-based contractility, albeit more slowly, in early fly embryos

(A) Micrographs illustrate MRLC-GFP in cycle 14 with drug vehicle (H_2O; n = 5 embryos), or with RhoA-GTPase inhibitors, Rhosin (n = 10) or exoenzyme C3 (n = 10). Cellularization is perturbed by the inhibition of RhoA, judged by the loss of myosin front (basal panels).

(B) In prior cycles 10–13, cytoplasmic compartments can form and divide even when RhoA is inhibited (n = 5 embryos in each condition). Cytoplasmic compartments that begin division in interphase (left; white or yellow arrows), as well as those that can divide without nuclei (right; white arrows), continued to occur in embryos where RhoA was inhibited.

(C) Violin plots compare cytoplasmic compartment size under indicated conditions (in cycle 12).

(D) Images illustrate myosin localization, either in control conditions (top panels; n = 5 embryos) or when injected with the Rho kinase inhibitor Y-27632 (n = 8 embryos).

(E and F) Images depict cytoplasmic compartment formation at the beginning of interphase (cycle 12) either in unperturbed embryos or in embryos injected with Y-27632. Note the delay in compartment formation under +Y-27632. See (I) and (J) for sample sizes.

(G) Violin plots compare cytoplasmic compartment size under indicated conditions derived from (E).

(H) In embryos injected with Y-27632 (n = 8 embryos), cytoplasmic compartments can still divide in interphase (left; white or yellow arrows in the apical channel, with arrowheads pointing at the associated nuclei in the basal channel). Cytoplasmic divisions can also continue without associated nuclei (mid-panels). Slower cytoplasmic compartment formation in Y-27632-injected embryos (as shown in E and F) occasionally leads to nuclear fusions in early interphase (right panels; white arrowhead).

(I and J) Bar charts quantify the compartment formation delays depicted in (E) and (F), respectively, along with the associated nuclear cycle length (cycle 12). Each data point in (C) and (G) represents an embryo (N), whose distributions are indicated with quartile lines derived from the underlying cytoplasmic compartment data (n) and a probability density estimation using the kernel plot. Data in (I) and (J) are presented mean ± SD, where each point represents a single embryo. Statistical significance was assessed using a Welch's t test (for Gaussian distributed data) or a Mann-Whitney test. Scale bars, 5 µm.

(Figure S7E; Video S5). Since $CycB^{+/-}$ embryos displayed ~35% genetic penetrance to induce mitotic delays in >5% of all nuclei (Figure 7H, light pink data points), we tested whether a more complete depletion of cyclin B would elicit higher penetrance. In embryos injected with dsRNA against cyclin B ($CycB^{RNAi}$; 10–15 min prior to cycle 10), we observed a remarkable penetrance in inducing mitotic-delay clusters (Figures S7F and S7G) for ~28% of all nuclei on average (Figure 7H). The $CycB^{RNAi}$ embryos also displayed a much higher fraction of early cytoplasmic divisions in interphase (Figure 7I), just as expected from a weakened

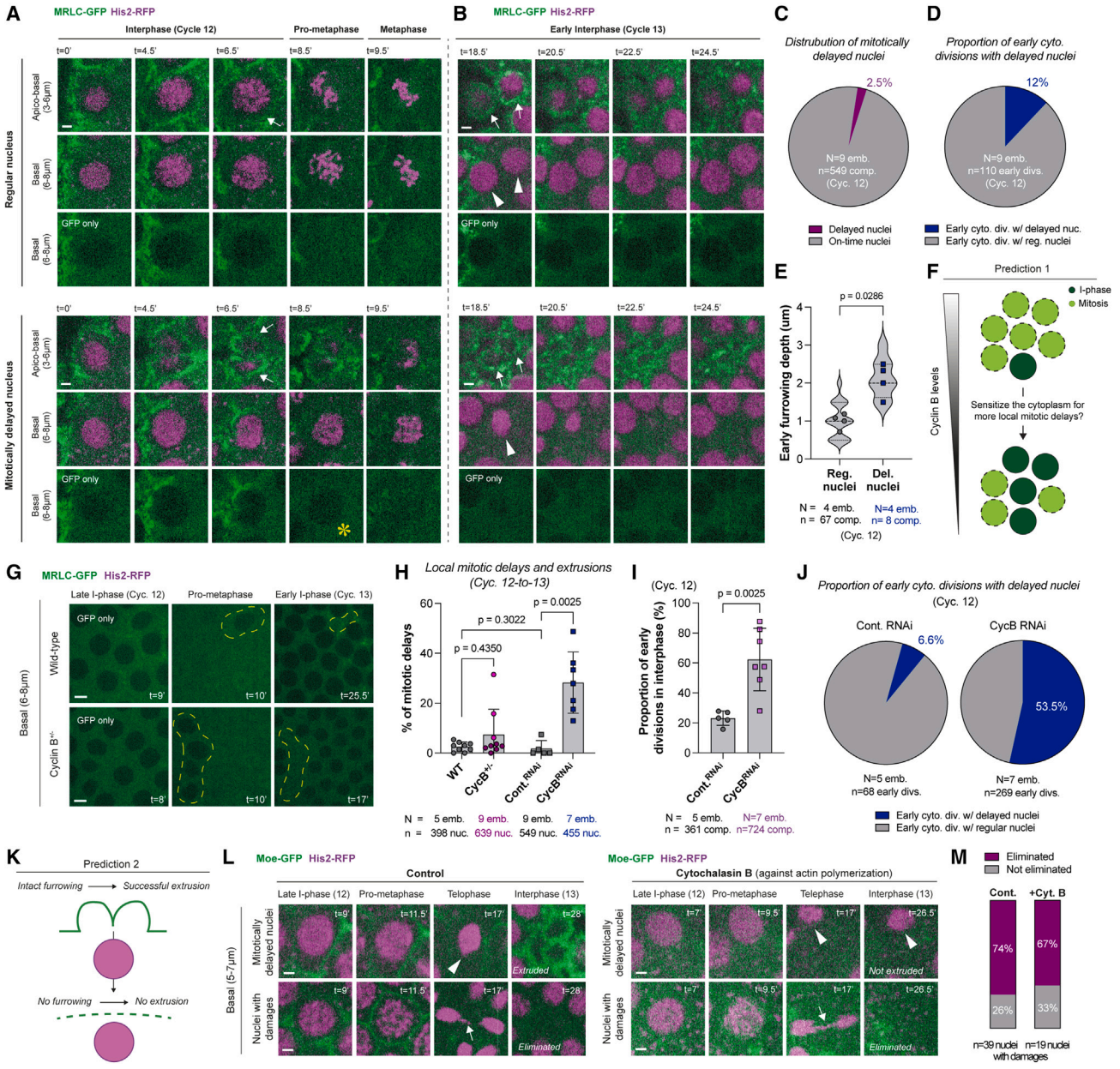

Figure 7. Autonomous cytoplasmic divisions help facilitate the extrusion of nuclei that locally delay into and slip mitosis during blastoderm formation

(A and B) Micrographs show a nucleus that enters mitosis on time (top set of panels) and one that is delayed into mitosis by 1.5–2 min locally (bottom set of panels). Scale bars, 2 μm. (A) Regular nuclei are typically in synchrony with their cytoplasmic compartments (white arrows; top). By contrast, delayed nuclei are associated with early cytoplasmic divisions in interphase (white arrows; bottom). See the visible delays in chromosome condensation and NEB (denoted by a yellow asterisk in the basal "GFP-only" panel). (B) At the beginning of the next cycle, although regular nuclei have divided and been encapsulated by their compartments (white arrowheads and arrows, respectively), delayed nuclei slip mitosis. Nevertheless, the cytoplasmic compartments associated with the delayed nuclei divided autonomously and appeared to extrude them basally.

(C and D) Pie charts display (C) the fraction of nuclei that locally delay into mitosis in unperturbed embryos expressing MRLC-GFP and His2-RFP, and (D) the proportion of early cytoplasmic divisions that are associated with mitotically delayed nuclei in the same embryos.

(E) Violin plots compare the furrowing depth of early cytoplasmic divisions at NEB in regular versus mitotically delayed nuclei.

(F) Cartoon illustrates the first prediction (see Results) of our working hypothesis on the mechanism of how mitotic delays are triggered and how the delayed nuclei are eliminated.

(G) Images show nuclear entry into mitosis in wild-type (WT) versus CycB$^{+/-}$ embryos, expressing MRLC-GFP and His2-RFP. Dashed yellow lines highlight delayed nuclei and their extrusions. To emphasize the mitotic delays, only the GFP channel was displayed (see Figures S7D and S7E, for a concomitant depiction of the two channels). Scale bars, 5 μm.

(legend continued on next page)

Cdk1 activity, exacerbating the decoupling between cytoplasmic and nuclear cycles. Importantly, a significantly higher fraction of the early dividing compartments coincided with the mitotically delayed nuclei in the CycB^{RNAi} embryos (Figure 7J), supporting the possibility that autonomous cytoplasmic divisions can help mediate the elimination of delayed nuclei. These results also support the notion that mitotically delayed nuclei and their eliminations are triggered more frequently by lower Cdk1 activity.

To test prediction 2 (Figure 7K), we examined nuclear elimination events in embryos injected with cytochalasin B, where the cytoplasmic compartments are fully abolished, but centrosome and nuclear cycles continue[26,66] (Figures S6G and S6H; Video S6) despite various karyotype abnormalities associated with DNA breakages and/or damages[67] (Figures 7L and S7A). Just as the control embryos, the cytochalasin B treated embryos (n = 6) had several nuclei that delayed into mitosis (Figure 7L; Video S7, white arrows labeled type 1). Remarkably, none of the delayed nuclei were eliminated (Figure 7L; Video S7). Conversely, nuclei with karyotype damages continued to be largely eliminated, like in the control embryos (Figures 7L and 7M; Video S7). Based on these results, we propose that autonomous cytoplasmic divisions may help facilitate the extrusion of mitotically delayed nuclei from the blastoderm.

DISCUSSION

Prevailing models in cell biology hold that the nucleus and mitotic CDK/cyclin complexes provide spatiotemporal cues essential for cytoplasmic divisions.[19,20] Our findings that the cytoplasm can compartmentalize and divide repeatedly without the nucleus and mitotic CDK/cyclin activity, challenge these long-held views and raise several key questions.

What could be the clock that governs the autonomous cytoplasmic division cycle?

Our findings point to a cytoplasmic division cycle that operates autonomously. We find that autonomous cytoplasmic divisions can occur twice as fast (~6.5 min) as the corresponding nuclear divisions (~15 min) in fly embryos (Figure 3H), suggesting that CDK/cyclins normally slow the cytoplasmic division cycle to couple it with the nuclear division cycle. By contrast, autonomous centriole duplication cycles occur at a natural period of ~20 min in this system, suggesting that mitotic CDK/cyclin complexes normally speed up centriole duplication cycles.[10] These findings provide compelling evidence for the emerging concept of autonomous clocks, in which CDK/cyclin complex is postulated to couple a network of autonomous biological cycles to run at the pace of nuclear cycles.[6,10,68,69]

We currently do not know the clock mechanism that governs cytoplasmic division cycles; however, our results reveal potential avenues to explore. For example, since a global translation shutdown does not appear to halt cytoplasmic divisions (Figures 2D and S2C), these cycles are likely governed by the cycles of a post-translational modification (PTM). Emerging evidence implicates critical regulatory roles for PTMs during cytoplasmic divisions.[70,71] These include Plk1 phosphorylations to regulate centrosome separation,[72,73] which is thought to provide geometric cues for timely furrowing.[74] We recently demonstrated that Plk4, a paralog of Plk1, acts as an autonomous clock to time centriole duplication cycles.[10] Here, Plk4's localization to centrioles enables its activation by auto-phosphorylation, so as to help time the growth of these organelles. Similarly, Plk1 is normally auto-inhibited until its recruitment to the centrosomes,[75–77] where this recruitment is sufficient to activate Plk1[78] by helping it release its auto-inhibition. As such, it will be intriguing to explore whether Plk1's localization to the centrosome could help initiate centrosome separation and time cytoplasmic divisions.

Could cytoplasmic divisions employ distinct MT organizers based on when the division cues emerge in the cell cycle?

Several MT organizers have been postulated to help transmit the division cues for the cytoplasm during the cell cycle.[34] Does the cytoplasm use mitotic or central spindles[38–40] to achieve this? Or, as Ray Rappaport had seminally argued, could centrosomal MTs do the same?[36,37] Alternatively, could it be a combination of both,[79,80] or either in redundant ways?[47,81–84] To date, there is no consensus as to which of these mechanisms dictate cytoplasmic divisions.[34,85] However, in all of these scenarios, it is commonly believed that the MT organizers must act in response to mitotic signals.

Together with recent reports that cleavage furrowing can be triggered to occur ectopically by biochemical[24] or genetic[86] means, our findings (Figure 3) imply that there are yet-to-be-identified cues that time cytoplasmic divisions independent of mitotic signals. When such division cues emerge during the cell cycle, cells must be able to use a readily available MT organizer to mediate cleavage furrowing. In developing embryos

(H) Bar charts quantify the population percentage of mitotically delayed nuclei and their extrusions in WT and CycB$^{+/-}$ embryos expressing MRLC-GFP and His2-RFP, or in embryos injected with scrambled dsRNA (Cont.^{RNAi}) or dsRNA against CycB. Three light pink data points in the CycB$^{+/-}$ indicate embryos with >5% mitotically delayed nuclei, highlighting the genetic penetrance of this response in heterozygous embryos (~35%).
(I) Bar graphs compare the proportion of cytoplasmic divisions that begin in interphase under indicated conditions.
(J) Pie charts show the fraction of early cytoplasmic divisions associated with delayed nuclei in Control^{RNAi} and CycB^{RNAi} embryos.
(K) The second prediction of our working hypothesis as indicated in (F).
(L) Panels illustrate the fate of mitotically delayed nuclei and nuclei with damages under control versus +cytochalasin B (expressing Moe-GFP and His2-RFP). White arrows denote the nuclear damages (lagging chromosomes in this case). Scale bars, 2 μm.
(M) Bars depict the proportion of karyotype-damaged nuclei that are eliminated, under control versus +cyctochalasin B.
All analyses (C)–(M) were performed in cycle 12. Each data point in (E) represents an embryo (N), whose distributions are indicated with quartile lines derived from the underlying furrow depth data (n) and a probability density estimation using the kernel plot. Data in (H) and (I) are presented mean ± SD, where each point represents a percentage average from a single embryo. Statistical significance was assessed using a Welch's t test (for Gaussian distributed data) or a Mann-Whitney test.
See also Figures S6 and S7.

where CDK/cyclin activity licenses mitotic MT organizers (e.g., the spindle), we find that the cytoplasmic divisions can occur without the centrosome, a principal organizer of interphase MTs (Figure 4). Conversely, when CDK/cyclin is inactive and mitotic MT organizers are unavailable, centrosomes become essential to sustain cytoplasmic divisions (Figures 5C–5E). Thus, the cytoplasmic cycle can employ distinct MT organizers to transmit its division cues based on their availability.

Based on these findings, we postulate the following model for how cells may decide which MT organizer to employ more predominantly during cytoplasmic divisions: in a regular mitotic cycle, CDK/cyclin is fully coupled to inhibit any furrowing until after chromosome segregation begins. As such, when the division cues emerge in anaphase, the central spindle could enable the furrowing process—as is normally done in many cell types.[19] However, if there is a slight uncoupling and the division cues emerge in metaphase instead, cells may leverage the mitotic spindle to kick-start the process. In a more extreme scenario, should the cytoplasmic divisions uncouple to start prior to mitosis, cells may employ the centrosomes. This model may provide a compelling new perspective on why cells might be primed to leverage distinct MT organizers to mediate cleavage furrowing: the ability to deploy the most readily available MT organizer based on when the division cues emerge during the cell cycle.

Could autonomous cytoplasmic divisions confer physiological advantages?

Here, we observed during unperturbed fly embryogenesis that a fraction of nuclei exhibits an apparent delay into mitosis locally (Figure 7). Despite this delay, cytoplasmic compartments divide autonomously and appear to eliminate the undivided nuclei by extrusion. These results suggest that autonomous cytoplasmic divisions might be a means by which nuclei that are unable to execute timely mitosis—presumably due to an undesired deficit(s)—are eliminated during blastoderm formation prior to morphogenesis.

Such extrusions in fly embryos are reminiscent of a minor fraction of roundworm embryonic cells that similarly stop cycling and are subsequently eliminated by an extrusion program, involving the downregulation of cell-cycle molecules.[87] In zebrafish embryos and canine epithelia, oncogene-transformed cells can also stall in prophase and occasionally extrude through an unusual division,[88] where a cytokinetic ring separates the basal and apical parts of the cell from epithelium. Although the upstream signals may vary among different animals, we postulate that the mechanisms might converge on a common pathway in development by leveraging autonomous divisions to preserve genome integrity and partitioning more generally.

Limitations of the study

Ablating multiple regions (>3–4) on the blastoderm can lead to dramatic wound responses. If it were technically feasible, it would be informative to ablate all centrosome pairs locally, to control whether the neighboring centrosomes somehow support the cytoplasmic compartments that divide without centrosomes. Nonetheless, we found that this is highly unlikely, as we can halt cytoplasmic divisions by ablating centrosomes in arrested embryos. Additionally, although we are tempted to ascribe the local delays and extrusions of nuclei (Figure 7) to upstream cellular stressors, we currently lack direct evidence on whether such nuclei pose defects that might be detrimental to physiology if they were not to be extruded. Finally, our study leverages fly embryogenesis as a model system to investigate cytoplasmic divisions. As for every cell type, this model has its unique and specialized set of requirements for cytoplasmic divisions. Future work will demonstrate whether the organizational principles proposed here apply to cytoplasmic divisions in other systems.

STAR★METHODS

Detailed methods are provided in the online version of this paper and include the following:

- KEY RESOURCES TABLE
- RESOURCE AVAILABILITY
  - Lead contact
  - Materials availability
  - Data and code availability
- EXPERIMENTAL MODEL AND STUDY PARTICIPANT DETAILS
  - *D. melanogaster* stocks and husbandry
- METHOD DETAILS
  - Microinjection experiments in embryos and unfertilized eggs
  - Drug inventory, purified enzymes and the synthesis of double-stranded RNA
  - Microscopy and image analysis
  - Förster Resonance Energy Transfer (FRET) measurements and analysis
  - Laser ablation experiments
- QUANTIFICATION AND STATISTICAL ANALYSIS

SUPPLEMENTAL INFORMATION

Supplemental information can be found online at https://doi.org/10.1016/j.cell.2023.09.010.

ACKNOWLEDGMENTS

We thank the Aydogan lab for insightful discussions. We are grateful to Daniel Kiehart, Patrick O'Farrell, Blake Riggs, and William Theurkauf for flies expressing Moe-GFP (Daniel Kiehart), His2-RFP (Patrick O'Farrell), UAS-Tom20-mCherry (Patrick O'Farrell), Pdi-GFP (Blake Riggs), and grp[fs1] (William Theurkauf). We thank Stefano Di Talia for sharing and advising us on the Cdk1-FRET construct. We thank the members of O'Farrell lab for their resourcefulness, both technically and conceptually. We thank Dominic Grisingher for checking whether our figures are color-blind friendly. We thank our friends whose discussions shaped this project from its inception to completion: Shelagh Campbell, Elif Nur Firat-Karalar, Fred Chang, Moumita Das, and Dyche Mullins. Our research is funded by NIH R35GM136420 (S.D.), NSF 1548297 Center for Cellular Construction (S.D.), Chan Zuckerberg Biohub (S.D.), Sandler Foundation Investigator Award (7029760; M.G.A.), NIH DP2GM154328 (M.G.A.), and UCSF PBBR NFR award (2017078; M.G.A.).

AUTHOR CONTRIBUTIONS

This study was conceptualized by A.B., F.E.I., and M.G.A. Investigation was done by A.B., F.E.I., A.A., M.R.-S., and M.G.A. Data were analyzed by A.B., F.E.I., A.A., and M.G.A. Methodology was developed by A.B., F.E.I., A.A., M.R.-S., S.D., and M.G.A. Project was administrated by M.G.A. Resources

were made by A.B., F.E.I., A.A., M.R.-S., S.D., and M.G.A. Software work was carried out by A.B., F.E.I., A.A., and M.G.A. Supervision was done by M.G.A. Validation experiments were carried out by A.B. and M.G.A. Main version of this manuscript was drafted by A.B., F.E.I., A.A., and M.G.A. with significant input from all authors. A.B., F.E.I., A.A., M.R.-S., S.D., and M.G.A. reviewed and edited the manuscript.

DECLARATION OF INTERESTS

The authors declare no competing interests.

INCLUSION AND DIVERSITY

We support inclusive, diverse, and equitable conduct of research.

Received: June 5, 2022
Revised: May 11, 2023
Accepted: September 12, 2023
Published: October 12, 2023

REFERENCES

1. Champion, L., Linder, M.I., and Kutay, U. (2017). Cellular reorganization during mitotic entry. Trends Cell Biol. *27*, 26–41. https://doi.org/10.1016/j.tcb.2016.07.004.
2. Stern, B., and Nurse, P. (1996). A quantitative model for the cdc2 control of S phase and mitosis in fission yeast. Trends Genet. *12*, 345–350.
3. Swaffer, M.P., Jones, A.W., Flynn, H.R., Snijders, A.P., and Nurse, P. (2016). CDK substrate phosphorylation and ordering the cell cycle. Cell *167*, 1750–1761.e16. https://doi.org/10.1016/j.cell.2016.11.034.
4. Loog, M., and Morgan, D.O. (2005). Cyclin specificity in the phosphorylation of cyclin-dependent kinase substrates. Nature *434*, 104–108. https://doi.org/10.1038/nature03329.
5. Kõivomägi, M., Valk, E., Venta, R., Iofik, A., Lepiku, M., Morgan, D.O., and Loog, M. (2011). Dynamics of Cdk1 substrate specificity during the cell cycle. Mol. Cell *42*, 610–623. https://doi.org/10.1016/j.molcel.2011.05.016.
6. Mofatteh, M., Echegaray-Iturra, F., Alamban, A., Dalla Ricca, F., Bakshi, A., and Aydogan, M.G. (2021). Autonomous clocks that regulate organelle biogenesis, cytoskeletal organization, and intracellular dynamics. eLife *10*, e72104. https://doi.org/10.7554/eLife.72104.
7. Jiménez, A., Lu, Y., Jambhekar, A., and Lahav, G. (2022). Principles, mechanisms and functions of entrainment in biological oscillators. Interface Focus *12*, 20210088. https://doi.org/10.1098/rsfs.2021.0088.
8. Gard, D.L., Hafezi, S., Zhang, T., and Doxsey, S.J. (1990). Centrosome duplication continues in cycloheximide-treated Xenopus blastulae in the absence of a detectable cell cycle. J. Cell Biol. *110*, 2033–2042. https://doi.org/10.1083/jcb.110.6.2033.
9. McCleland, M.L., and O'Farrell, P.H. (2008). RNAi of mitotic cyclins in Drosophila uncouples the nuclear and centrosome cycle. Curr. Biol. *18*, 245–254. https://doi.org/10.1016/j.cub.2008.01.041.
10. Aydogan, M.G., Steinacker, T.L., Mofatteh, M., Wilmott, Z.M., Zhou, F.Y., Gartenmann, L., Wainman, A., Saurya, S., Novak, Z.A., Wong, S.-S., et al. (2020). An autonomous oscillation times and executes centriole biogenesis. Cell *181*, 1566–1581.e27. https://doi.org/10.1016/j.cell.2020.05.018.
11. Al Jord, A., Shihavuddin, A., Servignat d'Aout, R., Faucourt, M., Genovesio, A., Karaiskou, A., Sobczak-Thépot, J., Spassky, N., and Meunier, A. (2017). Calibrated mitotic oscillator drives motile ciliogenesis. Science *358*, 803–806. https://doi.org/10.1126/science.aan8311.
12. Nanjundappa, R., Kong, D., Shim, K., Stearns, T., Brody, S.L., Loncarek, J., and Mahjoub, M.R. (2019). Regulation of cilia abundance in multiciliated cells. eLife *8*, e44039. https://doi.org/10.7554/eLife.44039.
13. Zielke, N., Edgar, B.A., and DePamphilis, M.L. (2013). Endoreplication. Cold Spring Harb. Perspect. Biol. *5*, a012948. https://doi.org/10.1101/cshperspect.a012948.
14. Raff, J.W., and Glover, D.M. (1988). Nuclear and cytoplasmic mitotic cycles continue in Drosophila embryos in which DNA synthesis is inhibited with aphidicolin. J. Cell Biol. *107*, 2009–2019. https://doi.org/10.1083/jcb.107.6.2009.
15. Clute, P., and Masui, Y. (1997). Microtubule dependence of chromosome cycles in Xenopus laevis blastomeres under the influence of a DNA synthesis inhibitor, aphidicolin. Dev. Biol. *185*, 1–13. https://doi.org/10.1006/dbio.1997.8540.
16. Ganier, O., Lutzmann, M., Cau, J., Peiffer, I., Lemmers, C., Zitouni, S., Theillet, C., and Méchali, M. (2020). Mitosis without DNA replication in mammalian somatic cells. https://doi.org/10.1101/2020.07.08.193607.
17. Chan, K.Y., Yan, C.-C.S., Roan, H.-Y., Hsu, S.-C., Tseng, T.-L., Hsiao, C.-D., Hsu, C.-P., and Chen, C.-H. (2022). Skin cells undergo asynthetic fission to expand body surfaces in zebrafish. Nature *605*, 119–125. https://doi.org/10.1038/s41586-022-04641-0.
18. Alberts, B., Johnson, A., Lewis, J., Raff, M., Roberts, K., and Walter, P. (2002). Molecular Biology of the Cell, Fourth Edition (Garland Science).
19. Pollard, T.D., and O'Shaughnessy, B. (2019). Molecular mechanism of cytokinesis. Annu. Rev. Biochem. *88*, 661–689. https://doi.org/10.1146/annurev-biochem-062917-012530.
20. Basant, A., and Glotzer, M. (2018). Spatiotemporal regulation of RhoA during cytokinesis. Curr. Biol. *28*, R570–R580. https://doi.org/10.1016/j.cub.2018.03.045.
21. Mitchison, T.J., and Field, C.M. (2021). Self-organization of cellular units. Annu. Rev. Cell Dev. Biol. *37*, 23–41. https://doi.org/10.1146/annurev-cellbio-120319-025356.
22. Lv, Z., de-Carvalho, J., Telley, I.A., and Großhans, J. (2021). Cytoskeletal mechanics and dynamics in the Drosophila syncytial embryo. J. Cell Sci. *134*, jcs246496. https://doi.org/10.1242/jcs.246496.
23. Foe, V.E., and Alberts, B.M. (1983). Studies of nuclear and cytoplasmic behaviour during the five mitotic cycles that precede gastrulation in Drosophila embryogenesis. J. Cell Sci. *61*, 31–70.
24. Crest, J., Concha-Moore, K., and Sullivan, W. (2012). RhoGEF and positioning of Rappaport-like furrows in the early drosophila embryo. Curr. Biol. *22*, 2037–2041. https://doi.org/10.1016/j.cub.2012.08.046.
25. Xie, Y., and Blankenship, J.T. (2018). Differentially-dimensioned furrow formation by zygotic gene expression and the MBT. PLoS Genet. *14*, e1007174. https://doi.org/10.1371/journal.pgen.1007174.
26. Foe, V.E., Field, C.M., and Odell, G.M. (2000). Microtubules and mitotic cycle phase modulate spatiotemporal distributions of F-actin and myosin II in Drosophila syncytial blastoderm embryos. Development *127*, 1767–1787. https://doi.org/10.1242/dev.127.9.1767.
27. Blake-Hedges, C., and Megraw, T.L. (2019). Coordination of embryogenesis by the centrosome in Drosophila melanogaster. In The Golgi Apparatus and Centriole: Functions, Interactions and Role in Disease Results and Problems in Cell Differentiation, M. Kloc, ed. (Springer International Publishing), pp. 277–321. https://doi.org/10.1007/978-3-030-23173-6_12.
28. Morgan, D.O. (2007). The Cell Cycle: Principles of Control (New Science Press).
29. Farrell, J.A., Shermoen, A.W., Yuan, K., and O'Farrell, P.H. (2012). Embryonic onset of late replication requires Cdc25 down-regulation. Genes Dev. *26*, 714–725. https://doi.org/10.1101/gad.186429.111.
30. Sibon, O.C.M., Stevenson, V.A., and Theurkauf, W.E. (1997). DNA-replication checkpoint control at the Drosophila midblastula transition. Nature *388*, 93–97. https://doi.org/10.1038/40439.
31. Deneke, V.E., Melbinger, A., Vergassola, M., and Di Talia, S. (2016). Waves of Cdk1 activity in S phase synchronize the cell cycle in drosophila embryos. Dev. Cell *38*, 399–412. https://doi.org/10.1016/j.devcel.2016.07.023.

32. Gavet, O., and Pines, J. (2010). Progressive activation of CyclinB1-Cdk1 coordinates entry to mitosis. Dev. Cell *18*, 533–543. https://doi.org/10.1016/j.devcel.2010.02.013.

33. Murray, A.W., and Kirschner, M.W. (1989). Cyclin synthesis drives the early embryonic cell cycle. Nature *339*, 275–280. https://doi.org/10.1038/339275a0.

34. Burgess, D.R., and Chang, F. (2005). Site selection for the cleavage furrow at cytokinesis. Trends Cell Biol. *15*, 156–162. https://doi.org/10.1016/j.tcb.2005.01.006.

35. Lee, K.-Y., Davies, T., and Mishima, M. (2012). Cytokinesis microtubule organisers at a glance. J. Cell Sci. *125*, 3495–3500. https://doi.org/10.1242/jcs.094672.

36. Rappaport, R. (1961). Experiments concerning the cleavage stimulus in sand dollar eggs. J. Exp. Zool. *148*, 81–89. https://doi.org/10.1002/jez.1401480107.

37. Rappaport, R. (1986). Establishment of the mechanism of cytokinesis in animal cells. Int. Rev. Cytol. *105*, 245–281. https://doi.org/10.1016/s0074-7696(08)61065-7.

38. Cao, L.G., and Wang, Y.L. (1996). Signals from the spindle midzone are required for the stimulation of cytokinesis in cultured epithelial cells. Mol. Biol. Cell *7*, 225–232. https://doi.org/10.1091/mbc.7.2.225.

39. Bonaccorsi, S., Giansanti, M.G., and Gatti, M. (1998). Spindle self-organization and cytokinesis during male meiosis in asterless mutants of Drosophila melanogaster. J. Cell Biol. *142*, 751–761. https://doi.org/10.1083/jcb.142.3.751.

40. Courthéoux, T., Reboutier, D., Vazeille, T., Cremet, J.-Y., Benaud, C., Vernos, I., and Prigent, C. (2019). Microtubule nucleation during central spindle assembly requires NEDD1 phosphorylation on serine 405 by Aurora A. Journal. J. Cell Sci. *132*, jcs231118. https://doi.org/10.1242/jcs.231118.

41. Aydogan, M.G., Wainman, A., Saurya, S., Steinacker, T.L., Caballe, A., Novak, Z.A., Baumbach, J., Muschalik, N., and Raff, J.W. (2018). A homeostatic clock sets daughter centriole size in flies. J. Cell Biol. *217*, 1233–1248. https://doi.org/10.1083/jcb.201801014.

42. Aydogan, M.G., Hankins, L.E., Steinacker, T.L., Mofatteh, M., Saurya, S., Wainman, A., Wong, S.-S., Lu, X., Zhou, F.Y., and Raff, J.W. (2022). Centriole distal-end proteins CP110 and Cep97 influence centriole cartwheel growth at the proximal end. J. Cell Sci. *135*, jcs260015. https://doi.org/10.1242/jcs.260015.

43. Rodrigues-Martins, A., Riparbelli, M., Callaini, G., Glover, D.M., and Bettencourt-Dias, M. (2007). Revisiting the role of the mother centriole in centriole biogenesis. Science *316*, 1046–1050. https://doi.org/10.1126/science.1142950.

44. Nabais, C., Pessoa, D., de-Carvalho, J., van Zanten, T., Duarte, P., Mayor, S., Carneiro, J., Telley, I.A., and Bettencourt-Dias, M. (2021). Plk4 triggers autonomous de novo centriole biogenesis and maturation. J. Cell Biol. *220*, e202008090. https://doi.org/10.1083/jcb.202008090.

45. Royou, A., Sullivan, W., and Karess, R. (2002). Cortical recruitment of nonmuscle myosin II in early syncytial Drosophila embryos. J. Cell Biol. *158*, 127–137. https://doi.org/10.1083/jcb.200203148.

46. Menant, A., and Karess, R.E. (2012). Inducing "cytokinesis" without mitosis in unfertilized Drosophila eggs. Cell Cycle *11*, 2856–2863. https://doi.org/10.4161/cc.21190.

47. Dechant, R., and Glotzer, M. (2003). Centrosome separation and central spindle assembly act in redundant pathways that regulate microtubule density and trigger cleavage furrow formation. Dev. Cell *4*, 333–344. https://doi.org/10.1016/s1534-5807(03)00057-1.

48. Agircan, F.G., Schiebel, E., and Mardin, B.R. (2014). Separate to operate: control of centrosome positioning and separation. Philos. Trans. R. Soc. Lond. B Biol. Sci. *369*, 20130461. https://doi.org/10.1098/rstb.2013.0461.

49. De Simone, A., Nédélec, F., and Gönczy, P. (2016). Dynein transmits polarized actomyosin cortical flows to promote centrosome separation. Cell Rep. *14*, 2250–2262. https://doi.org/10.1016/j.celrep.2016.01.077.

50. Wu, J., and Akhmanova, A. (2017). Microtubule-organizing centers. Annu. Rev. Cell Dev. Biol. *33*, 51–75. https://doi.org/10.1146/annurev-cellbio-100616-060615.

51. Heald, R., Tournebize, R., Habermann, A., Karsenti, E., and Hyman, A. (1997). Spindle assembly in Xenopus egg extracts: respective roles of centrosomes and microtubule self-organization. J. Cell Biol. *138*, 615–628. https://doi.org/10.1083/jcb.138.3.615.

52. Khodjakov, A., Cole, R.W., Oakley, B.R., and Rieder, C.L. (2000). Centrosome-independent mitotic spindle formation in vertebrates. Curr. Biol. *10*, 59–67. https://doi.org/10.1016/s0960-9822(99)00276-6.

53. Mahoney, N.M., Goshima, G., Douglass, A.D., and Vale, R.D. (2006). Making microtubules and mitotic spindles in cells without functional centrosomes. Curr. Biol. *16*, 564–569. https://doi.org/10.1016/j.cub.2006.01.053.

54. Hayward, D., Metz, J., Pellacani, C., and Wakefield, J.G. (2014). Synergy between multiple microtubule-generating pathways confers robustness to centrosome-driven mitotic spindle formation. Dev. Cell *28*, 81–93. https://doi.org/10.1016/j.devcel.2013.12.001.

55. Théry, M., Racine, V., Pépin, A., Piel, M., Chen, Y., Sibarita, J.-B., and Bornens, M. (2005). The extracellular matrix guides the orientation of the cell division axis. Nat. Cell Biol. *7*, 947–953. https://doi.org/10.1038/ncb1307.

56. Kiyomitsu, T., and Cheeseman, I.M. (2012). Chromosome- and spindle-pole-derived signals generate an intrinsic code for spindle position and orientation. Nat. Cell Biol. *14*, 311–317. https://doi.org/10.1038/ncb2440.

57. Pollard, T.D. (2017). Nine unanswered questions about cytokinesis. J. Cell Biol. *216*, 3007–3016. https://doi.org/10.1083/jcb.201612068.

58. Cao, J., Albertson, R., Riggs, B., Field, C.M., and Sullivan, W. (2008). Nuf, a Rab11 effector, maintains cytokinetic furrow integrity by promoting local actin polymerization. J. Cell Biol. *182*, 301–313. https://doi.org/10.1083/jcb.200712036.

59. Crawford, J.M., Harden, N., Leung, T., Lim, L., and Kiehart, D.P. (1998). Cellularization in Drosophila melanogaster is disrupted by the inhibition of rho activity and the activation of Cdc42 function. Dev. Biol. *204*, 151–164. https://doi.org/10.1006/dbio.1998.9061.

60. Sullivan, W., Minden, J.S., and Alberts, B.M. (1990). daughterless-abo-like, a Drosophila maternal-effect mutation that exhibits abnormal centrosome separation during the late blastoderm divisions. Development *110*, 311–323. https://doi.org/10.1242/dev.110.2.311.

61. Sullivan, W., Daily, D.R., Fogarty, P., Yook, K.J., and Pimpinelli, S. (1993). Delays in anaphase initiation occur in individual nuclei of the syncytial *Drosophila* embryo. Mol. Biol. Cell *4*, 885–896.

62. Rothwell, W.F., Fogarty, P., Field, C.M., and Sullivan, W. (1998). Nuclear-fallout, a Drosophila protein that cycles from the cytoplasm to the centrosomes, regulates cortical microfilament organization. Development *125*, 1295–1303. https://doi.org/10.1242/dev.125.7.1295.

63. Takada, S., Kelkar, A., and Theurkauf, W.E. (2003). Drosophila checkpoint kinase 2 couples centrosome function and spindle assembly to genomic integrity. Cell *113*, 87–99. https://doi.org/10.1016/s0092-8674(03)00202-2.

64. Iampietro, C., Bergalet, J., Wang, X., Cody, N.A.L., Chin, A., Lefebvre, F.A., Douziech, M., Krause, H.M., and Lécuyer, E. (2014). Developmentally regulated elimination of damaged nuclei involves a Chk2-dependent mechanism of mRNA nuclear retention. Dev. Cell *29*, 468–481. https://doi.org/10.1016/j.devcel.2014.03.025.

65. Marzluff, W.F., and Duronio, R.J. (2014). Genome stress response in early development. Dev. Cell *29*, 375–376. https://doi.org/10.1016/j.devcel.2014.05.010.

66. Stevenson, V., Hudson, A., Cooley, L., and Theurkauf, W.E. (2002). Arp2/3-dependent Psuedocleavage furrow assembly in syncytial drosophila embryos. Curr. Biol. *12*, 705–711. https://doi.org/10.1016/S0960-9822(02)00807-2.

67. Mammel, A.E., and Hatch, E.M. (2022). Genome instability from nuclear catastrophe and DNA damage. Semin. Cell Dev. Biol. *123*, 131–139. https://doi.org/10.1016/j.semcdb.2021.03.021.

68. Lu, Y., and Cross, F.R. (2010). Periodic cyclin-Cdk activity entrains an autonomous Cdc14 release oscillator. Cell *141*, 268–279. https://doi.org/10.1016/j.cell.2010.03.021.

69. Özsezen, S., Papagiannakis, A., Chen, H., Niebel, B., Milias-Argeitis, A., and Heinemann, M. (2019). Inference of the high-level interaction topology between the metabolic and cell-cycle oscillators from single-cell dynamics. Cell Syst. *9*, 354–365.e6. https://doi.org/10.1016/j.cels.2019.09.003.

70. Bohnert, K.A., and Gould, K.L. (2011). On the cutting edge: post-translational modifications in cytokinesis. Trends Cell Biol. *21*, 283–292. https://doi.org/10.1016/j.tcb.2011.01.006.

71. Nguyen, L.T.S., and Robinson, D.N. (2020). The unusual suspects in cytokinesis: fitting the pieces together. Front. Cell Dev. Biol. *8*, 441.

72. Mardin, B.R., Agircan, F.G., Lange, C., and Schiebel, E. (2011). Plk1 controls the Nek2A-PP1γ antagonism in centrosome disjunction. Curr. Biol. *21*, 1145–1151. https://doi.org/10.1016/j.cub.2011.05.047.

73. Wellard, S.R., Zhang, Y., Shults, C., Zhao, X., McKay, M., Murray, S.A., and Jordan, P.W. (2021). Overlapping roles for PLK1 and Aurora A during meiotic centrosome biogenesis in mouse spermatocytes. EMBO Rep. *22*, e51023. https://doi.org/10.15252/embr.202051023.

74. Minc, N., Burgess, D., and Chang, F. (2011). Influence of cell geometry on division-plane positioning. Cell *144*, 414–426. https://doi.org/10.1016/j.cell.2011.01.016.

75. Seong, Y.-S., Kamijo, K., Lee, J.-S., Fernandez, E., Kuriyama, R., Miki, T., and Lee, K.S. (2002). A spindle checkpoint arrest and a cytokinesis failure by the dominant-negative Polo-box domain of Plk1 in U-2 OS Cells*210. J. Biol. Chem. *277*, 32282–32293. https://doi.org/10.1074/jbc.M202602200.

76. Jang, Y.-J., Lin, C.-Y., Ma, S., and Erikson, R.L. (2002). Functional studies on the role of the C-terminal domain of mammalian polo-like kinase. Proc. Natl. Acad. Sci. USA *99*, 1984–1989. https://doi.org/10.1073/pnas.042689299.

77. Elia, A.E.H., Rellos, P., Haire, L.F., Chao, J.W., Ivins, F.J., Hoepker, K., Mohammad, D., Cantley, L.C., Smerdon, S.J., and Yaffe, M.B. (2003). The molecular basis for phosphodependent substrate targeting and regulation of Plks by the Polo-box domain. Cell *115*, 83–95. https://doi.org/10.1016/S0092-8674(03)00725-6.

78. Xu, J., Shen, C., Wang, T., and Quan, J. (2013). Structural basis for the inhibition of Polo-like kinase 1. Nat. Struct. Mol. Biol. *20*, 1047–1053. https://doi.org/10.1038/nsmb.2623.

79. Murata-Hori, M., and Wang, Y.L. (2002). Both midzone and astral microtubules are involved in the delivery of cytokinesis signals: insights from the mobility of aurora B. Journal of Cell Biology *159*, 45–53. J. Cell Biol. *159*, 45–53. https://doi.org/10.1083/jcb.200207014.

80. Bringmann, H., and Hyman, A.A. (2005). A cytokinesis furrow is positioned by two consecutive signals. Nature *436*, 731–734. https://doi.org/10.1038/nature03823.

81. Rieder, C.L., Khodjakov, A., Paliulis, L.V., Fortier, T.M., Cole, R.W., and Sluder, G. (1997). Mitosis in vertebrate somatic cells with two spindles: implications for the metaphase/anaphase transition checkpoint and cleavage. Proc. Natl. Acad. Sci. USA *94*, 5107–5112. https://doi.org/10.1073/pnas.94.10.5107.

82. von Dassow, G. (2009). Concurrent cues for cytokinetic furrow induction in animal cells. Trends Cell Biol. *19*, 165–173. https://doi.org/10.1016/j.tcb.2009.01.008.

83. Baruni, J.K., Munro, E.M., and von Dassow, G. (2008). Cytokinetic furrowing in toroidal, binucleate and anucleate cells in C. elegans embryos. J. Cell Sci. *121*, 306–316. https://doi.org/10.1242/jcs.022897.

84. Su, K.-C., Bement, W.M., Petronczki, M., and von Dassow, G. (2014). An astral simulacrum of the central spindle accounts for normal, spindle-less, and anucleate cytokinesis in echinoderm embryos. Mol. Biol. Cell *25*, 4049–4062. https://doi.org/10.1091/mbc.E14-04-0859.

85. Verma, V., Mogilner, A., and Maresca, T.J. (2019). Classical and emerging regulatory mechanisms of cytokinesis in animal cells. Biology *8*, 55. https://doi.org/10.3390/biology8030055.

86. Wagner, E., and Glotzer, M. (2016). Local RhoA activation induces cytokinetic furrows independent of spindle position and cell cycle stage. J. Cell Biol. *213*, 641–649. https://doi.org/10.1083/jcb.201603025.

87. Dwivedi, V.K., Pardo-Pastor, C., Droste, R., Kong, J.N., Tucker, N., Denning, D.P., Rosenblatt, J., and Horvitz, H.R. (2021). Replication stress promotes cell elimination by extrusion. Nature *593*, 591–596. https://doi.org/10.1038/s41586-021-03526-y.

88. Anton, K.A., Kajita, M., Narumi, R., Fujita, Y., and Tada, M. (2018). Src-transformed cells hijack mitosis to extrude from the epithelium. Nat. Commun. *9*, 4695. https://doi.org/10.1038/s41467-018-07163-4.

89. Royou, A., Field, C., Sisson, J.C., Sullivan, W., and Karess, R. (2004). Reassessing the role and dynamics of nonmuscle myosin II during furrow formation in early drosophila embryos. Mbo *C 15*, 838–850. https://doi.org/10.1091/mbc.e03-06-0440.

90. Dobbelaere, J., Josué, F., Suijkerbuijk, S., Baum, B., Tapon, N., and Raff, J. (2008). A genome-wide RNAi screen to dissect centriole duplication and centrosome maturation in Drosophila. PLoS Biol. *6*, e224. https://doi.org/10.1371/journal.pbio.0060224.

91. Mavrakis, M., Rikhy, R., and Lippincott-Schwartz, J. (2009). Plasma membrane polarity and compartmentalization are established before cellularization in the fly embryo. Dev. Cell *16*, 93–104. https://doi.org/10.1016/j.devcel.2008.11.003.

92. Rogers, G.C., Rusan, N.M., Peifer, M., and Rogers, S.L. (2008). A multicomponent assembly pathway contributes to the formation of acentrosomal microtubule arrays in interphase Drosophila cells. Mol. Biol. Cell *19*, 3163–3178. https://doi.org/10.1091/mbc.e07-10-1069.

93. Callan, M.A., Cabernard, C., Heck, J., Luois, S., Doe, C.Q., and Zarnescu, D.C. (2010). Fragile X protein controls neural stem cell proliferation in the Drosophila brain. Hum. Mol. Genet. *19*, 3068–3079. https://doi.org/10.1093/hmg/ddq213.

94. Clarkson, M., and Saint, R. (1999). A His2AvDGFP fusion gene complements a lethal His2AvD mutant allele and provides an in vivo marker for Drosophila chromosome behavior. DNA Cell Biol. *18*, 457–462. https://doi.org/10.1089/104454999315178.

95. Jürgens, G., Wieschaus, E., Nüsslein-Volhard, C., and Kluding, H. (1984). Mutations affecting the pattern of the larval cuticle inDrosophila melanogaster: II. Zygotic loci on the third chromosome. Wilehm. Roux. Arch. Dev. Biol. *193*, 283–295. https://doi.org/10.1007/BF00848157.

96. Edgar, B.A., and O'Farrell, P.H. (1989). Genetic control of cell division patterns in the Drosophila embryo. Cell *57*, 177–187. https://doi.org/10.1016/0092-8674(89)90183-9.

97. Walt Disney Animation Studios. Physically based shading at Disney Walt Disney Animation Studios. https://disneyanimation.com/publications/physically-based-shading-at-disney/.

98. Alvarez-Rodrigo, I., Steinacker, T.L., Saurya, S., Conduit, P.T., Baumbach, J., Novak, Z.A., Aydogan, M.G., Wainman, A., and Raff, J.W. (2019). Evidence that a positive feedback loop drives centrosome maturation in fly embryos. eLife *8*, e50130. https://doi.org/10.7554/eLife.50130.

99. Miura, K. (2020). Bleach correction ImageJ plugin for compensating the photobleaching of time-lapse sequences. F1000Res *9*, 1494. https://doi.org/10.12688/f1000research.27171.1.

100. Elting, M.W., Hueschen, C.L., Udy, D.B., and Dumont, S. (2014). Force on spindle microtubule minus ends moves chromosomes. J. Cell Biol. *206*, 245–256. https://doi.org/10.1083/jcb.201401091.

STAR★METHODS

KEY RESOURCES TABLE

REAGENT or RESOURCE	SOURCE (or reference #)	IDENTIFIER
Chemicals, peptides, and recombinant proteins		
Voltalef grade H10S oil	Arkema	N/A
RNase*Zap*™	Thermo Fisher Scientific	Cat#AM9780
Cycloheximide	Sigma-Aldrich	Cat#01810
Colchicine	Sigma-Aldrich	Cat#C9754
Rhosin Hydrochloride	R&D Systems	Cat#5003/10
Y-27632	Adipogen	Cat#AG-CR1-3564
Cytochalasin B	ACROS Organics	Cat#228090010
Roscovitine	SelleckChem	Cat#S1153
Nocodazole	Sigma-Aldrich	Cat#M1404
Exoenzyme C3 transferase purified protein	Cytoskeleton Inc	Cat#CT03-A
Experimental models: Organisms/strains		
D. melanogaster: MRLC-GFP	Royou et al.[89] and Dobbelaere et al.[90]	FlyBase ID: FBal0221190
D. melanogaster: His2(Av)-RFP	Laboratory of P. O'Farrell	FlyBase ID: FBst0023650
D. melanogaster: Moe(-ABD)-GFP (Sqh promoter)	Laboratory of D. Kiehart	N/A
D. melanogaster: UAS-Toll-Venus	Mavrakis et al.[91]	FlyBase ID: FBst0030898
D. melanogaster: V32-Gal4	Bloomington Drosophila Stock Centre	FlyBase ID: FBtp0009293
D. melanogaster: Pdi-GFP (protein trap line Pdi^{G00198})	Laboratory of B. Riggs	FlyBase ID: FBal0147689
D. melanogaster: UAS-Tom20-mCherry	Laboratory of P. O'Farrell	N/A
D. melanogaster: V37-Gal4	Bloomington Drosophila Stock Centre	FlyBase ID: FBtp0016395; RRID: BDSC_7063
D. melanogaster: Sas-6-GFP	Aydogan et al.[41]	FlyBase ID: FBtp0131375
D. melanogaster: MRLC-mCherry	Bloomington Drosophila Stock Centre	FlyBase ID: FBti0164920; RRID_59024
D. melanogaster: mCherry-Sas-6	Rogers et al.[92]	FlyBase ID: FBal0366905
D. melanogaster: dlg1-GFP	Bloomington Drosophila Stock Centre	FlyBase ID: FBst0050859
D. melanogaster: Jupiter-mCherry	Callan et al.[93]	N/A
D. melanogaster: His2(Av)-GFP	Clarkson and Saint[94]	FlyBase ID: FBal0104781
D. melanogaster: UAS-Plk4	Rodrigues-Martins et al.[43]	FlyBase ID: FBtp0036898
D. melanogaster: Cdk1-FRET	Deneke et al.[31]	FlyBase ID: FBtp0141644
D. melanogaster: stg[7B] (Cdc25 amorphic allele)	Jürgens et al.[95] and Edgar and O'Farrell[96]	FlyBase ID: FBal0247234
D. melanogaster: grp[fs1] (Chk1 null allele)	Sibon et al.[30]	FlyBase ID: FBal0216722
D. melanogaster: MRLC-GFP / +; His2-RFP / +	This paper	N/A
D. melanogaster: His2-RFP / +; Moe-GFP / +	This paper	N/A
D. melanogaster: His2-RFP / V32-Gal4; UAS-Toll-Venus / +	This paper	N/A
D. melanogaster: + / +; Pdi-GFP / MRLC-mCherry	This paper	N/A
D. melanogaster: MRLC-GFP / +; UAS-Tom20-mCherry / V37-Gal4	This paper	N/A
D. melanogaster: Sas-6-GFP / +; MRLC-mCherry / +	This paper	N/A

(*Continued on next page*)

Continued

REAGENT or RESOURCE	SOURCE (or reference #)	IDENTIFIER
D. melanogaster: Sas-6-GFP / +; Jupiter-mCherry	This paper	N/A
D. melanogaster: dlg1-GFP / +;; Sas-6-mCherry / +	This paper	N/A
D. melanogaster: MRLC-GFP / +; Jupiter-mCherry / +	This paper	N/A
D. melanogaster: + / +; Moe-GFP / Jupiter-mCherry	This paper	N/A
D. melanogaster: UAS-Plk4 / V32-Gal4; Sas-6-GFP / MRLC-mCherry	This paper	N/A
D. melanogaster: UAS-Plk4 / V32-Gal4; Sas-6-GFP / Jupiter-mCherry	This paper	N/A
D. melanogaster: dlg1-GFP / +; His2-RFP / +	This paper	N/A
D. melanogaster: dlg1-GFP / +;; Jupiter-mCherry / +	This paper	N/A
D. melanogaster: Cdk1-FRET / +; MRLC-mCherry / +	This paper	N/A
D. melanogaster: grp[fs1] / grp[fs1]; MRLC-GFP / His2-RFP	This paper	N/A
D. melanogaster: + / +; MRLC-GFP / His2-RFP	This paper	N/A
D. melanogaster: MRLC-GFP / +; His2-RFP / stg[7B]	This paper	N/A
Oligonucleotides		
dsRNA against Cyclin A: 5'-TACAATTGCAAGC AGAAAGAGGATGAGCACCAGCAGCCGGATAT TAATACTAAATCGAACGTGAATTTGTTTTATAA GTTTTAAGTGTTTTGAGCCGCTGTCATGGCCA AATTGTATATTAGTTTAGTGTTTCCATGTAACAT TATGTAGTTTTAGTTATAAGTGTACACAATGGA TCAATTGCAGTTCGGTCGCAGTCAGCCAGTC GTATAAAAGCTTCGCATTGGTTGGCCGATTGA CAAGCTCCCGTTGCAAGTGCCGGACAATTTTA TATGTAAGCCATATAAAAGATAGTTGCCAAAAT ATACGCGCTTAACAACATTCGCGTCTGTCCAC GGTGAGAGCTTGTCATGCCAAGCGGGAGCAG TAAGAACTTCGGCAGTCTTAAAAACTATCCGA TTAGCCAATTGAAATTGGAGGAAGCCACCGG ACACAACATATTAGTGCTGCTTATGCTAACGA TATTTTATATTTCAACCTCTTTATGTTAAGTATG TATGTTTTCGTGTTTATAAATTGAACCATACTAA CGTATACAATGTGTCTAAAGCAGAAACAGCTA GCTTCGAGAATTATTTTACCATATTTATATATTA CTATTTACTCCGTAAATGTTCTGTGAACTCC-3'	RNA Greentech LLC	N/A
dsRNA against Cyclin B: 5'-CTACAACAAGTA CCAGGGCAGCAAGTTCCAGAAGATCGCGC TGCGAACGGAGCTGACCGGTGCGCTGATG GACTCGATTGTGGGCCAGAGCCAGAGGAA ATAGTGCGGTCCAAGGCGGACTGGAAGAC CCTGACTTACCTAGTTTAGTTTAATTTGTTTT CATTTTTAAATTTGTAGCGTATTTCATTTTCT GTTCGTTTCGTGTTCGTTAAAAAATGCGTAT AGTTACCGTAGTCGCATTGCCAACTATCTT TACCTGCATCACCCATCCCTAAGATATCGT AATCTGCTGGAGTCCCTTGAGCAGTTTTCG GCTACTGCCAAGAGCTGGCTCCGGCATCT TTGCCCACGGAGCACAAGTTGCTCGCGAG CCGGCCGCTGGGAGTGAGTTCCTCCGGTA AGACTAGGAACCGAACTAAACTGGAGCCC GTCAGCTCCTTTCGCTGGGTCACCATCTCA GTGGGAGCGAGCGGCGGAGCGGTGGACA CCGAGAGAGAGAGTGGGCAACGAGTTCAT TTGCTGGCCGAACACATCGGCGTTGTCTC TCCAAGAATTA-3'	RNA Greentech LLC	N/A

(*Continued on next page*)

Continued

REAGENT or RESOURCE	SOURCE (or reference #)	IDENTIFIER
dsRNA against Cyclin B3: 5'-CGCCAT GGATATATTCAACTACCTCAAAGTGC GCGAAGCGGAATTCCCCATTGCCGA CTATATGCCCAGGCAGATCCATCTG ACCACCTGGATGCGCACCCTGTTGG TCGACTGGATGGTGGAGGTGCAGGA AACGTTCGAGCTGAACCACGAGACT CTGTACCTAGCGGTTAAGATCGTCG ATCTGTATCTCTGCCGCGAGGTGATC AACAAAGAGAAGCTGCAACTTCTGG GCGCCGCTGCCTTCTTTATTGCCTG CAAGTACGATGAGCGACAGCCGCCG CTTATAGAGGATTTTTTGTATATCTGC GATGGTGCTTATAATCACGACGAGCT GGTGCGAATGGAGCGGGAGACGCT GCGCGTTATCAAGTACGATCTGGGC ATCCCGCTCTCGTACCGTTTCCTGC GCCGCTATGCCCGATGCGCCAAGG TGCCTATGCCCACGCTGACCCTGGC TCGATACATCCTGGAATTGTCGCTCA TGGATTACGCCAATATTTCGTTC-3'	RNA Greentech LLC	N/A
Scrambled dsRNA sequence: 5'-GAAT GCCGGGAACTTACGGAGTCAGGCGG CGCTGGATTCAGGGCGCGCCAACTC GAACCTCGGTCGACTAGACTGAGCG CCTGGTCAGGCCAGTCTAGGGCCTG GCGCGGCGTTACAACGGTCGGTCGA CCTCTGCGGAGGCGCCAAACATGCC ACACGTCTTTAAAGCCGATTTTTTCAG AATGCCTGCACGATGATTCGGACTCT TCGGTCGACCCAGGCCAGGAGTTTC TCAGCGCGACGTTTGCCCGCCTAGT GAAGTCTCCGATAGAGCAAGGTGGG CTAACCAATGCGTTCAACCTCCCCAC ACACGGGTATTCGTGGCACGCATAG GCCATTGGACCGTGGCATCCTCCGTT CGGGGTATCAGCACACGACCGGCAT GCCTTAGGGGTTACCGACGCGTGGT GCAGTGCTGCGCGTCCCGTCAAATT ATCTATCCCTCACTATCGCGTCCCAC TAACGCTTCGTCTCGAGATGGTGCCC CGGGCTAGGGGATC-3'	RNA Greentech LLC	N/A
Software and algorithms		
Volocity 6.3	Perkin Elmer	RRID: SCR_002668
μmanager	Open Source: www.micro-manager.org	RRID: SCR_016865
MetaMorph 7.7.8.0	Molecular Devices	RRID: SCR_002368
Fiji (ImageJ)	National Institutes of Health	RRID: SCR_003070
Python	Python Software Foundation	RRID: SCR_008394
Prism 9	GraphPad	RRID: SCR_002798
Blender 3.4	Open Source: www.blender.org	RRID: SCR_008606
Principle Volume Shader	Walt Disney Animation Studios[97]	N/A
Original Blender files and resources here	This paper	https://figshare.com/s/3b9a0beeb0e3c20c8690
Python script to generate 3D renders of fly embryo images	This paper	https://github.com/Aydogan-Laboratory/stack-to-openvdb
Python script to quantity FRET measurements	This paper	https://github.com/Aydogan-Laboratory/Cdk1-FRET-Calculation

RESOURCE AVAILABILITY

Lead contact

Further information and requests for resources and reagents should be directed to and will be fulfilled by the lead contact, Mustafa G. Aydogan (mustafa.aydogan@ucsf.edu).

Materials availability

Availability of all the materials in this study, including chemicals, oligonucleotides and *D. melanogaster* strains generated here are indicated throughout the STAR Methods and key resources table. Requests for materials should be directed to and will be fulfilled by the lead contact.

Data and code availability

All microscopy data and experimental materials are immediately available upon request.

- Original Blender files for microscopy visualization are deposited at FigShare repository with its accession link listed in the key resources table. Requests for data otherwise should be directed to and will be fulfilled by the lead contact.
- Python scripts to generate 3D renders of the fly embryo images and to quantify FRET measurements are deposited at GitHub with their accession links listed in the key resources table. All otherwise equations and codes generated for this study are indicated throughout the STAR Methods.
- Any additional information required to reanalyze the data reported in this paper is available from the lead contact upon request.

EXPERIMENTAL MODEL AND STUDY PARTICIPANT DETAILS

D. melanogaster stocks and husbandry

Since this study uses *Drosophila* embryogenesis as its model system, it only utilizes 5-10 days old adult female flies as its experimental subject. Flies for experiments were kept at 25°C in *Drosophila* culture medium (7.5% molasses, 1.01% agar, 1.4% agar, 5.6% cornmeal,.75% tegosept,.23% propionic acid,.04% phosphoric acid) in vials or bottles. Stocks were kept in 8x 2.5cm plastic vials. The specific fly alleles used in this study are listed in key resources table. The fly stocks generated and tested in this study are also listed in key resources table.

METHOD DETAILS

Microinjection experiments in embryos and unfertilized eggs

Embryos were incubated at 25°C and harvested from juice plates containing 25% cranberry-raspberry juice, made from 2% sucrose and 1.8% agar, with the addition of fresh yeast droplets.

After a 20min collection with juice plates, embryos were aged at 25°C for 50 minutes (so as to begin the injections starting from earlier nuclear cycles, such as cyc. 9–11). After this incubation period, embryos were dechorionated using clear double-sided tape, and mounted on a strip of glue onto a 35mm MatTek glass-bottom petri dish with a 14mm microwell. After desiccation for 6min at 25°C, the embryos were then covered in *Voltalef* oil (Grade H10S). All drug, purified enzyme and dsRNA injections were performed using a borosilicate glass tube, 1.2mm outer diameter, 0.9 mm inner diameter, pulled on a model P-87 micropipette puller. The heat, pull, velocity, and time values were 670, 60, 80, 190 respectively. Unperturbed or vehicle-injected embryos were subjected to same treatments except the injection.

As previously described,[10] the ''early'' injection of Cyclin A-B-B3 dsRNA cocktail (but not for the ''late'' injection of Cyclin B dsRNA only) was performed on embryos that were collected after a 20min incubation time – a method that successfully arrests the nuclear divisions of fly embryos in the earliest cycles it could. For the triple cyclin dsRNA cocktail experiments, the embryos were injected with a final needle concentration of 0.67 mg/ml. For the cyclin B dsRNA experiments, the embryos were injected with a needle concentration of 2 mg/ml. During the injections, all surfaces (including the pipettes) were cleaned with RNase*Zap*™ RNase decontamination solution (ThermoFisher Scientific) and 70% ethanol. Following the injections, the arrested embryos were left to age for 1-1.5h before imaging.

For unfertilized egg experiments, the specimen was collected during a 2h incubation with juice plates at 25°C, then were imaged immediately. For unfertilized eggs where *de novo* centrioles were produced, the specimen was collected during a 2h incubation with juice plates, then were aged at 25°C for another 1-2h before imaging, or before injecting first and imaging afterwards.

Drug inventory, purified enzymes and the synthesis of double-stranded RNA

Following drugs were dissolved in nuclease-free water, kept at -20°C and injected at the needle concentration of: Cycloheximide (50ug/mL; Sigma-Aldrich), Colchicine (100ug/mL; Sigma-Aldrich), Rhosin Hydrochloride (19.6mg/mL; R&D Systems) and Y-27632 (76mM; Adipogen). Following drugs were dissolved in DMSO (ranging from 50-100% in stock solution), kept at -20°C, and injected at the needle concentration of: Cytochalasin B (11.7mg/mL; ACROS Organics), Roscovitine (10mM; SelleckChem) and Nocodazole

(10mg/mL; Sigma Aldrich). Purified Exoenzyme C3 transferase protein (Cytoskeleton Inc) was prepared with nuclease free water, kept at -80°C and injected at a needle concentration of 100ug/uL.

dsRNAs were synthesized by RNA Greentech LLC (Texas, USA) and stored at -80°C. Coding sequences used to generate the dsRNAs are listed in key resources table. To cross-confirm the validity of the correct RNA product in house, the dsRNAs were ran on electrophoresis (1.5% agarose gel) using 2xRNA loading buffer (ThermoFisher Scientific). For electrophoresis, a 1:1 mixture of loading buffer and dsRNA was heated to 65°C for 5 min and then was transferred to ice to decompose any secondary structure on the dsRNA.

Microscopy and image analysis

Imaging specifications

Live embryos were imaged at room temperature with two systems running the Volocity software: either a spinning disk confocal system (Perkin Elmer Ultraview), using an Olympus IX70 microscope with a planApo 60x 1.40 NA oil immersion objective; or another spinning disk confocal system (VT-QLC100 VisiTech International), using a Leica DM-IRB microscope with a HCX PL APO 63x 1.40 NA oil immersion objective. Running the μmanager software, we also alternatively used another spinning disk confocal system (CSU10 Yokogawa), using a Nikon Eclipse Ti-E microscope with a perfect focus system, equipped with a 60x 1.4 NA oil immersion objective. In all these scope options, control versus experimental groups were always kept within the same system to maintain consistency. Either 481 and 561 (Leica), or 488 and 561 (Olympus and Nikon), nm lasers were used to visualize GFP/Venus and RFP/mCherry in multiple fly lines. Using 0.5μm intervals, 20 slices were obtained every 30 seconds. All videos were captured with emission discrimination with corresponding filters.

3D-rendering and image display of early fly embryos

Confocal volumes were rendered in Blender 3.4 using the raytracing engine *Cycles* (see our Blender files and resources here: https://figshare.com/s/3b9a0beeb0e3c20c8690). Micrographs from z-stacks were first bleach-corrected in ImageJ. Subsequently, they were exported into a file complying the OpenVDB volumetric format using a script developed in house (https://github.com/Aydogan-Laboratory/stack-to-openvdb). These volumetric files were imported to Blender using the option to add OpenVDB files. Volumes were shaded using a principled volume shader[97] for MRLC, and a Lambertian emission shader His2. The intensity of emission and principled volume shaders were fine-tuned manually; Blender files with exported volumes are included in Video S1 and Figure 1B for further inspection. Volumes were framed using an orthographic camera in order to maintain relative distances and were rendered using a 1:1 aspect ratio. Kymographs were extracted from this procedure by restricting the rendering volume to a subset of the original volumetric file.

Scoring cytoplasmic divisions that occur early in interphase, or those that occur without nuclei, both in space and time

Images were analyzed in ImageJ-Fiji. To score the fraction of cytoplasmic compartments that divided in interphase, each compartment was judged by an expert viewer (A.B. and A.A.), to see if they divide early or not, based on the following criteria: **1)** a complete stripe of the cytoplasmic boundary marker (e.g. MRLC-GFP) must bisect the cytoplasmic compartment, indicative of division (see Figure 1B for example). **2)** The cytoplasmic division furrow must remain stable over time. **3)** The division furrow occurs prior to mitotic entry, as judged by invasion of MRLC-GFP into the nucleoplasm. Percentage proportions were calculated as the number of early cytoplasmic divisions divided by the total number of cytoplasmic compartments that were inspected within each embryo. When the cytoplasm divided early through the criteria above, the time by which the cytoplasm initiates its division was also scored simultaneously. This is the timepoint when the cytoplasmic division boundary first forms. In a parallel vein, cytoplasmic compartments that divided without nuclei were scored visually by examining the absence of nuclei in all the basal channels that were scored (see Figure 2A for the extent of basal depth).

Cytoplasmic compartment size measurements

Compartment size measurements were performed in Fiji by using the free area selection tools to determine the outer boundaries of the cytoplasm (as defined by markers such as MRCL or Moe-ABD tagged with a fluorescent marker) and measuring the area of these regions of interest by conventional measurement tools available in ImageJ.

Period measurements

The period of autonomous cytoplasmic divisions in embryos injected with dsRNA against all the mitotic cyclins, or with cycloheximide, was measured by scoring the division-to-division times. This was done for multiple compartments in the two consecutive generations after the first appearance of compartments in the triple cyclin dsRNA experiments (coming from embryos expressing MRLC-GFP and Jupiter-mCherry). The same protocol was followed, but starting from the first arrested interphase (cycle 10), in cycloheximide experiments (using embryos expressing MRLC-GFP and His2-RFP).

Total cell cycle duration in embryos (that cycle normally) was measured by calculating the time from the start of interphase (when the nuclear envelope reforms) till the end of telophase (when the dividing daughter nuclei separate). Interphase durations were measured in a similar way, but only till the time of nuclear envelope breakdown instead of the end of telophase.

Radial profiles and line scan plots

For the laser ablation experiments in Figure 4D, radial profiles were plotted in ImageJ to quantify the fluorescence signal associated with astral MTs (Jupiter-mCherry) and centrioles (Sas-6-GFP) associated with the spindle poles in metaphase. A previously published protocol[98] was roughly followed and modified to achieve this. As such, measurements were performed on a 6μm-long line, positioned orthogonally to the elongating axis of the mitotic spindles. Control profiles (unablated groups) were always taken from the

immediate neighbours of the ablated centrosome pairs. Background signals (the mean signal of a 6x6μm region) were quantified locally and independently in the vicinity of each of our measurements, and subtracted from the profiles before normalization. For each unablated centrosomes profile, the peaks (at 0μm) were normalized to 1 arbitrary unit (A.U.) for both the channels, then the normalization factor (to scale down to 1 A.U.) was applied to the intensities in the ablation profiles accordingly.

For the line scan plots in Figures S2F and S2G, the above protocol was largely applied, in which a line of interest, ranging between 8–10μm, was positioned orthogonal to the division furrows, encompassing organelles within. To plot the signals, background subtraction was performed using a rolling ball radius of 50 pixels. Plots were smoothened by a median filter with a 2-pixel radius for ease of visualization.

Scoring the elimination of mitotically delayed nuclei or nuclei with karyotype damages

Mitotic delays were judged by the delay of nuclear envelope breakdown (in MRLC-GFP channel) and chromatin condensation (in His2-RFP channel). Nuclear damages were judged largely by assessing whether chromatin took up the phenotypes similar to those listed in Figure S7A. Both the delay-dependent extrusions and nuclear damage-dependent eliminations were judged by alternating the z-slices.

Furrow depth measurements

For early cytoplasmic divisions and nuclear extrusion analyses, furrow depth measurements were performed by alternating the z-stacks and recording corresponding values. To determine relative times for the formation of cytoplasmic compartments in control embryos and in embryos injected with Rho Kinase inhibitor Y-27632, the incidents were determined by visual examinations for when >50% of the compartments were formed in the cytoplasm. A similar approach was taken to judge the time of cytoplasmic divisions in embryos injected with cycloheximide.

Förster Resonance Energy Transfer (FRET) measurements and analysis

A previously published Cdk1 FRET biosensor was used to measure the dynamics of Cdk1 activity oscillations. Briefly, the biosensor has an mCerulean donor fluorophore and a YPet acceptor fluorophore connected by a phosphobinding Polo-box domain, as well as a 16 amino acid residue that is phosphorylated by Cdk1. For measuring FRET, samples were imaged at room temperature on a Leica DM IRB inverted microscope, equipped with a spinning disk (VT-QLC100 VisiTech International) and a 63x 1.40 NA oil immersion objective through the Volocity software (Perkin Elmer).

Using embryos that express Cdk1-FRET and MRLC-mCherry constructs, three different excitation/emission combinations were used to acquire FRET measurements in conjunction with MRLC dynamics. To image MRLC-mCherry, we excited the sample with a 565 nm laser and used a 605/50 emission filter (C1). To measure the extent of FRET, we excited with a 436 nm laser and used a 545/40 emission filter (C2). To measure the donor fluorophore, we excited with a 436 nm laser and used a 483/32 emission filter (C3). We used an exposure time of 350ms for each channel and imaged an 8μm stack at 1μm intervals.

Images were pre-processed in FIJI. First, a position in the z-axis was selected such that the centriolar structures, which are also labelled by the biosensor, was in focus. Quantification was then done using a Python script (deposited at https://github.com/Aydogan-Laboratory/Cdk1-FRET-Calculation). To account for photobleaching, we measured the mean fluorescence intensity for each time frame. The time series was then fit to a double exponential decay function and corrected per the following equation[99]:

$$I'_t = \frac{A_1+A_2+B}{A_1e^{-\tau_1 t}+A_2e^{-\tau_2 t}+B} I_t$$

where I'_t and I_t are, respectively, the corrected and raw mean intensity values of the channel at time t; A_1 and A_2 are initial scaling factors; τ_1 and τ_2 are time constants; and B is a baseline correction factor.

The parameters A_1, A_2, τ_1, τ_2, and Bwere acquired by fitting the timeseries to a double exponential decay function using SciPy's *curve_fit* function:

$$f(t) = B + \sum_{1}^{2} A_i e^{-\tau_i t}$$

The ratio between the corrected mean fluorescence intensity of the two channels was then calculated as:

$$Emission\ Ratio = \frac{C2_{corr}}{C3_{corr}}$$

To facilitate the comparison of dynamics, the emission ratio was then normalized to the first timepoint acquired in our videos.

Laser ablation experiments

For laser ablation experiments, samples were imaged using an inverted microscope (Eclipse Ti-E; Nikon) with a spinning disk confocal (CSU-X1; Yokogawa Electric Corporation), head dichroic Semrock Di01-T405/488/568/647 for multicolor imaging, equipped with 405 nm (100 mW), 488 nm (120mW), 561 nm (150mW), and 642 nm (100mW) diode lasers, emission filters ET455/50M, ET525/50M, ET630/75M and ET690/50M for multicolor imaging, and an iXon3 camera (Andor Technology) operated by MetaMorph (7.7.8.0; Molecular Devices).[100] Embryos were imaged with a 60x 1.40 Ph3 oil objective. Laser ablation (30-40 pulses

of 3 ns at 20 Hz) with 514 nm light was performed using the MicroPoint Laser System (Andor), and the same system but with 405nm light was used to perform the *bleaching* control experiments. Embryos were imaged every 15s with a single stack before ablation, and every 15s with multiples stacks after ablation (0.8μm step size, 11 steps, 8μm total range).

Achieving full ablation at the blastoderm was not immediately straightforward. Due to the embryo's cytoplasmic flows, centrioles can move laterally (even as fast as >10um per 30 sec), making it difficult to target them for an extended period. When these movements happened and the centrioles left the intended region during ablation, Sas-6-GFP signal was inadvertently bleached, but quickly recovered afterwards (Figure S5A; t=1'-2' highlighted by *white* arrows), indicating ablation failure. To control for this interpretation, we used a laser line with a shorter wavelength (405 nm) to intentionally bleach the centrioles without ablating them. Just as was the case for centrioles that drifted away (Figure S5A), the signal on bleached centrioles recovered quickly (Figure S5B; t=1'-3.5' highlighted by *white* arrows), and even more significantly in the next cell cycle (t=7.5' highlighted by *white* arrows).

Successful centriole ablations were thus verified by the immediate elimination of the Sas-6-GFP signal (centrioles were targeted repeatedly until complete elimination of the signal), and by the subsequent absence of Sas-6-GFP signal recovery in the consecutive timepoints. As demonstrated previously,[41,42] the Sas-6-GFP cartwheel structure grows linearly during early/mid interphase in fly embryos, so the dynamics of centriole growth served as a positive control for proper ablation (failing a proper ablation, the fluorescence would recover within 1-1.5min). Therefore, the centriole ablations were done in early interphase. In case of laser ablations in arrested embryos (injected with the dsRNA cocktail), a similar protocol was followed.

Finally, since centrioles are positioned close (5–10μm) to the cortical blastoderm, even slight increases of laser power (to maintain robust ablation) can cause dramatic membrane-injury. We were successful in ablating centrioles without damaging the cortex in 5 out of 20 trials in cycling embryos, and 5 out of 9 trials in arrested embryos. The embryos with injured membranes were excluded from analysis.

QUANTIFICATION AND STATISTICAL ANALYSIS

All measurements in the main text, figures and legends are represented as Mean±SD. The details for quantification, statistical significance, sample size, definitions of centers, and the measures for dispersion/precision are indicated in the main body and corresponding figure legends. Statistical significance was defined by $p<0.05$. To determine distribution normality, data were subjected to D'Agostino-Pearson normality test. GraphPad Prism 9 was used for all statistical analyses.

CellPress
OPEN ACCESS

Supplemental figures

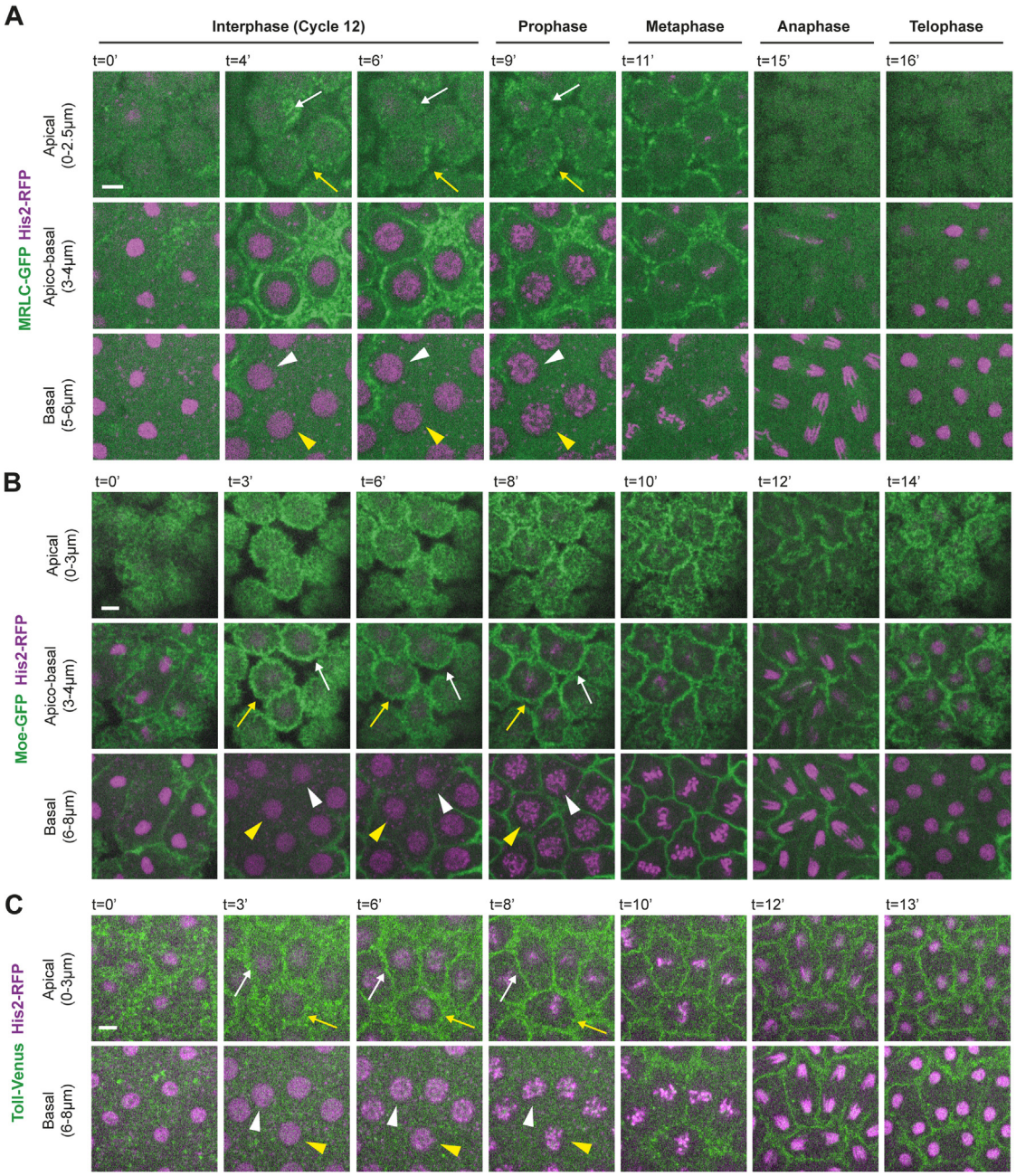

Figure S1. Nuclei in early fly blastoderm are usually contained within single cytoplasmic compartments, which typically do not divide till the end of mitosis, related to Figure 1

(A–C) Micrographs illustrate the progression of interphase and entry into mitosis during cycle 12 in embryos expressing His2-RFP (marking chromosomes) simultaneously with (A) MRLC-GFP (myosin), (B) Moe-GFP (binding actin filaments), or (C) Toll-Venus (plasma membrane). Top panels (apical) visualize the cytoplasmic compartments (marked by the actomyosin walls and plasma membrane), highlighted by white and/or yellow arrows. Bottom panels (basal) depict the nuclei that reside in each compartment, highlighted by white and/or yellow arrowheads. Scale bars, 5 µm.

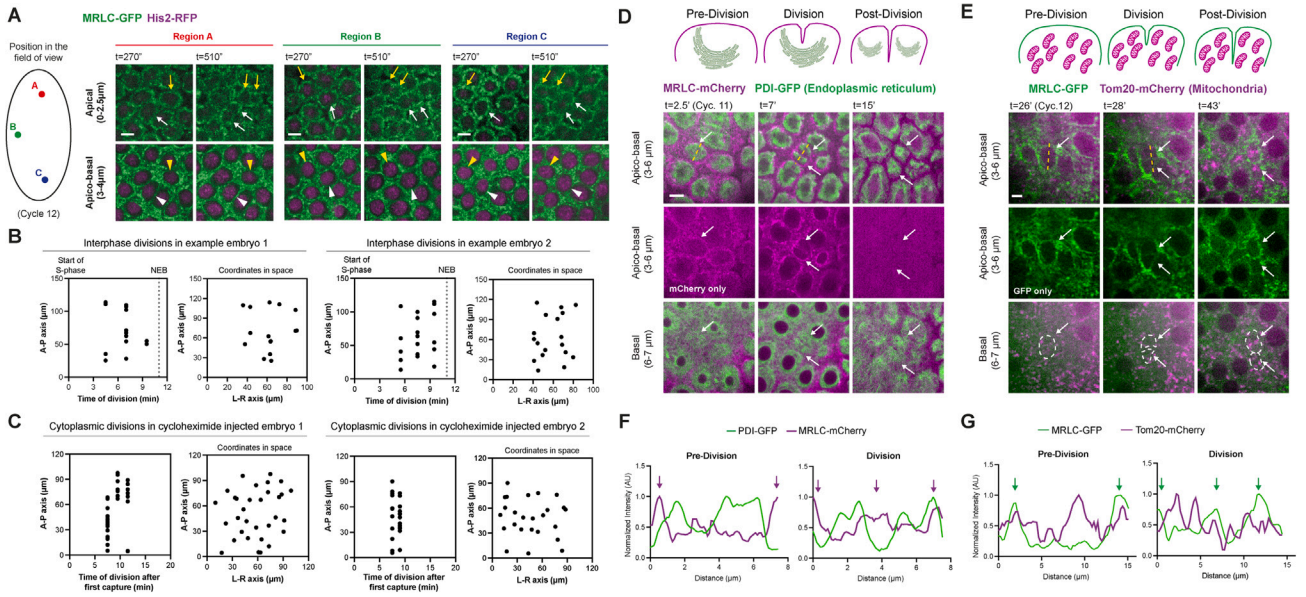

Figure S2. Spatiotemporal properties of cytoplasmic divisions when uncoupled from nuclei and their divisions, related to Figures 1 and 2

(A) Micrographs from different regions in the same field of view (denoted with red, green, and blue fonts) show cytoplasmic compartments in early interphase (left) and their nearly simultaneous start of divisions in space and time (right panels). White and yellow arrows highlight example cytoplasmic compartments, and the arrowheads with corresponding colors show their arrested nuclei. Representative panels are from (n = 9) control embryos (in cycle 12). Scale bars, 5 μm.

(B and C) In a pair of example single embryos, scatter plots (left) quantify the anterior-posterior (A-P) position of interphase cytoplasmic divisions as a function of time during the cell cycle, respectively, for (B) control and (C) cycloheximide-injected embryos (see Figure 2D for examples of cytoplasmic divisions in cycloheximide-injected embryos, where n = 5 independent repeats). t = 0′ marks the start of interphase in the control embryos and of interphase arrest capture in embryos injected with cycloheximide. NEB marks the beginning of mitosis. Similarly, the plots on the right quantify the position of interphase cytoplasmic divisions across A-P and left-right (L-R) axes of embryos. Note how interphase cytoplasmic divisions do not cluster into local regions, indicating that a more global program is likely to synchronize these events.

(D and E) Time-lapse micrographs show (D) the endoplasmic reticulum (ER; signified by an ER resident protein disulfide-isomerase [PDI] tagged with GFP) and (E) the mitochondria (marked by a mitochondrial translocase of the outer membrane [Tom20] tagged with mCherry), residing in cytoplasmic compartments that divide without nuclei (MRLC with a complementary fluorescent tag). Cytoplasmic divisions are highlighted by white arrows. See how the ER and mitochondria are nearly equally segregated between the daughter cytoplasmic compartments after the cytoplasmic division. In (E), white dashed lines in the basal panels signify the boundary of the cytoplasm as seen from the apical-basal view. Cartoons above illustrate a schematic interpretation of the data.

(F and G) Line scans of (F) PDI-GFP and (G) Tom20-mCherry fluorescence intensity orthogonal to the division axis of cytoplasmic compartments (yellow dashed lines in D and E) before (left) or during (right) the cytoplasmic division. The two peaks—(F) in the MRLC-mCherry curve or (G) in the MRLC-GFP curve (pre-division)—delineate the boundaries of the cytoplasm (magenta or green arrows, respectively, left graphs). During the division, however, a furrow forms, bisecting the compartment, as indicated by the third peak in the middle, signified by magenta (F) or green (G) arrows (right graphs). In (F), prior to the cytoplasmic division, the ER is enclosed within the two peaks. After division, the ER is segregated evenly and remains enclosed by the two daughter cytoplasmic compartments. In (G), the Tom20-mCherry peak indicates the presence of mitochondria within the compartment. After division, like in (F), a third peak appears, representing the new furrow. More local spikes in the Tom20-mCherry intensity are also observed, showing that mitochondria are retained within compartments during division. Data for (D)–(G) are representative from 3 independent embryos for each genotype. Scale bars, 5 μm.

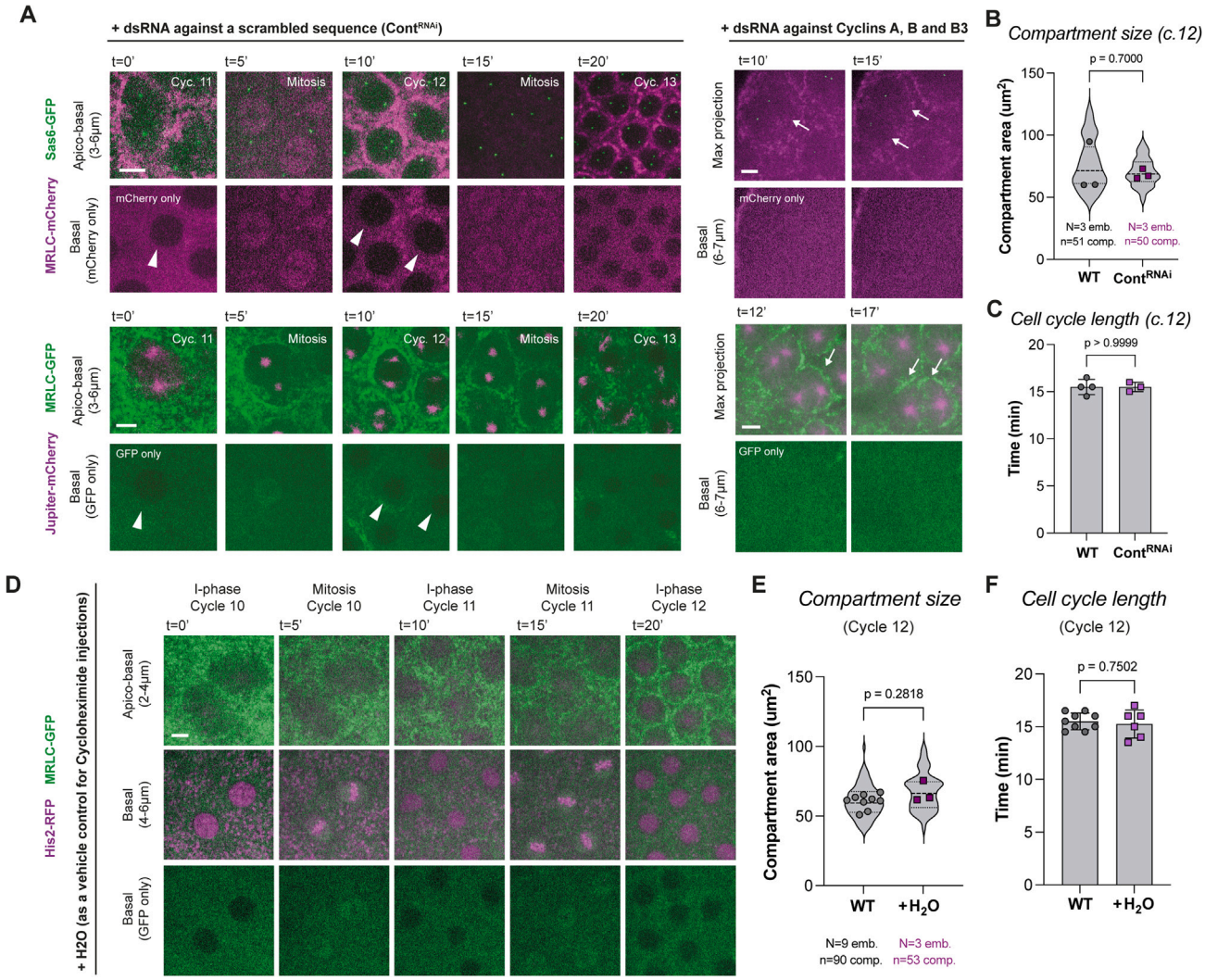

Figure S3. Control experiments for dsRNA and cycloheximide injection experiments, related to Figures 2 and 3

(A) Micrographs show that injecting dsRNA against a scrambled sequence (left) do not lead to any obvious defects in early embryogenesis. On the right panels, images demonstrate the autonomous cytoplasmic divisions in embryos injected with the cyclin A-B-B3 triple cocktail dsRNA. Illustrated by white arrows in the max-projection panels, see the formation and division of compartments without nuclei. As performed previously using the nuclear retention of Plk4-mNeonGreen and mCherry-Sas-6,[10] the lack of nuclei was controlled by examining the back-illumination of MRLC-GFP or MRLC-mCherry channels in basal z-slices, because nuclei normally appear as dark circle shadows in these channels in cycling embryos—see in embryos injected with scrambled dsRNA ($Cont^{RNAi}$), where white arrowheads highlight examples of nuclei that are associated with the cytoplasmic compartments in the top panel. The max-projection images in the dsRNA micrographs are retrieved directly from Figure 3A for cross-comparison. n = 3 independent scrambled dsRNA experiments per each genotype. n = 5 and 13 triple cyclin dsRNA experiments for Sas-6-GFP and Jupiter-mCherry groups, respectively.

(B) Violin plots compare the sizes of cytoplasmic compartments between unperturbed (WT) and $Cont^{RNAi}$ embryos, expressing MRLC-GFP and Jupiter-mCherry (in cycle 12).

(C) Bar graphs compare the total cell-cycle length (cycle 12) in the same embryos as in (B).

(D) Time-lapse micrographs reveal that H_2O injections (as a vehicle control for cycloheximide) do not lead to any obvious defects in early embryogenesis, as the embryos (n = 6) go through their cleavage and nuclear divisions relatively normally.

(E and F) Same as (B) and (C), but between unperturbed embryos (cycle 12) and embryos injected with H_2O, expressing MRLC-GFP and His2-RFP.

Each data point in (B) and (E) represents an embryo (N), whose distributions are indicated with quartile lines derived from the underlying compartment data (n) and a probability density estimation using the kernel plot. Data in (C) and (F) are presented as mean ± SD, where each point represents a single embryo. Statistical significance was assessed using a Welch's t test (for Gaussian distributed data) or a Mann-Whitney test. Scale bars, 5 µm.

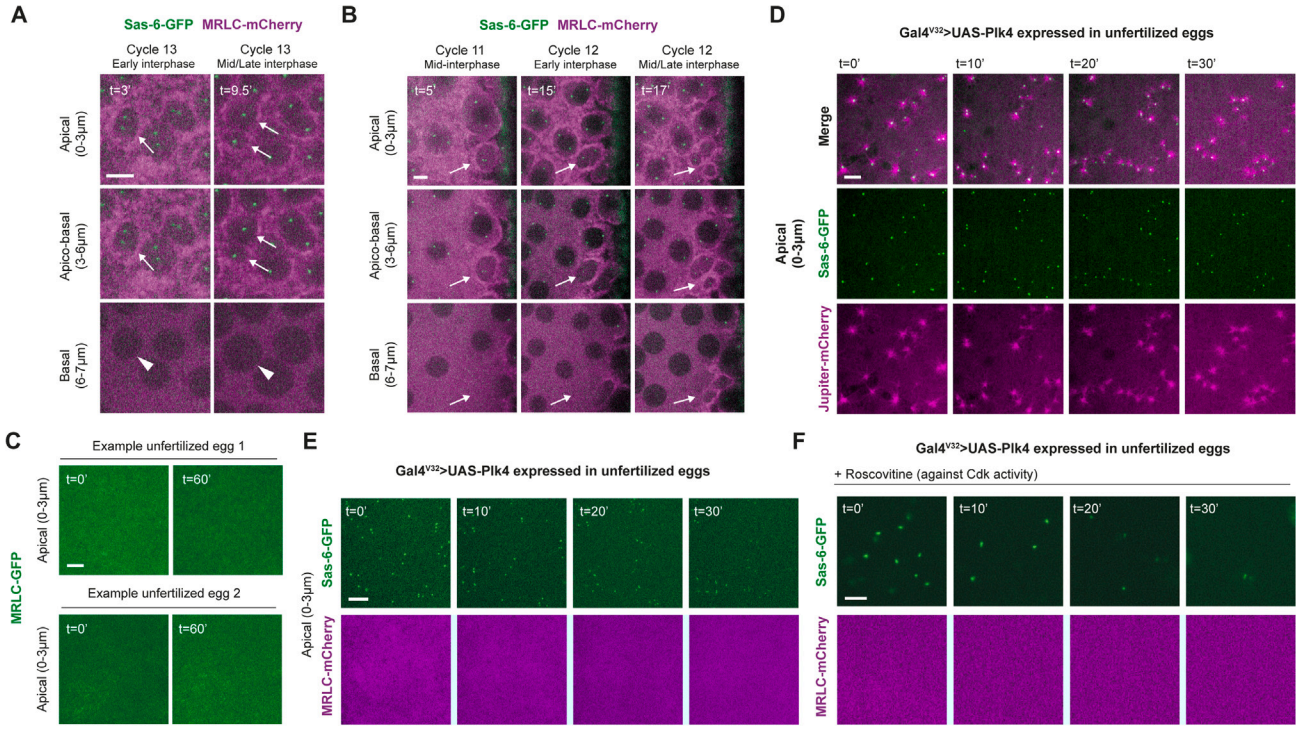

Figure S4. Although centrioles are tightly associated with cytoplasmic compartments, genetically inducing *de novo* centrosome biogenesis is not sufficient to trigger the formation of cytoplasmic compartments in unfertilized eggs, related to Figure 4

(A) Images show centrioles (Sas-6-GFP) in a cytoplasmic compartment (MRLC-mCherry) that divides in interphase (indicated by white arrows). White arrowheads point at the corresponding nucleus that has not entered mitosis.

(B) Time-lapse panels show centrioles in cytoplasmic compartments that divide without any resident nucleus. White arrows aid following the cytoplasmic divisions apically and the absence of nuclei basally.

(C) Micrographs are obtained from a pair of example unfertilized eggs expressing MRLC-GFP, illustrating that the *Drosophila* egg cytoplasm does not self-organize into compartments by default, even with the passage of time (n = 6 embryos).

(D) Micrographs depict that the genetically induced *de novo* centrioles (with Gal4^{V32} > UAS-Plk4 expression) mature into centrosomes in unfertilized eggs, evident from their nucleation of MTs (marked by Jupiter-mCherry). Panels are representative time series from n = 11 embryos.

(E and F) Images show that inducing *de novo* centrosomes in unfertilized eggs is not sufficient to trigger the formation of cytoplasmic compartments, even with the passage of time. This is true both in unperturbed eggs (n = 5 embryos) and in eggs injected with Roscovitine (n = 8 embryos) to inhibit Cdk1 activity, which is normally refractory for myosin localization.[45] Scale bars, 5 μm.

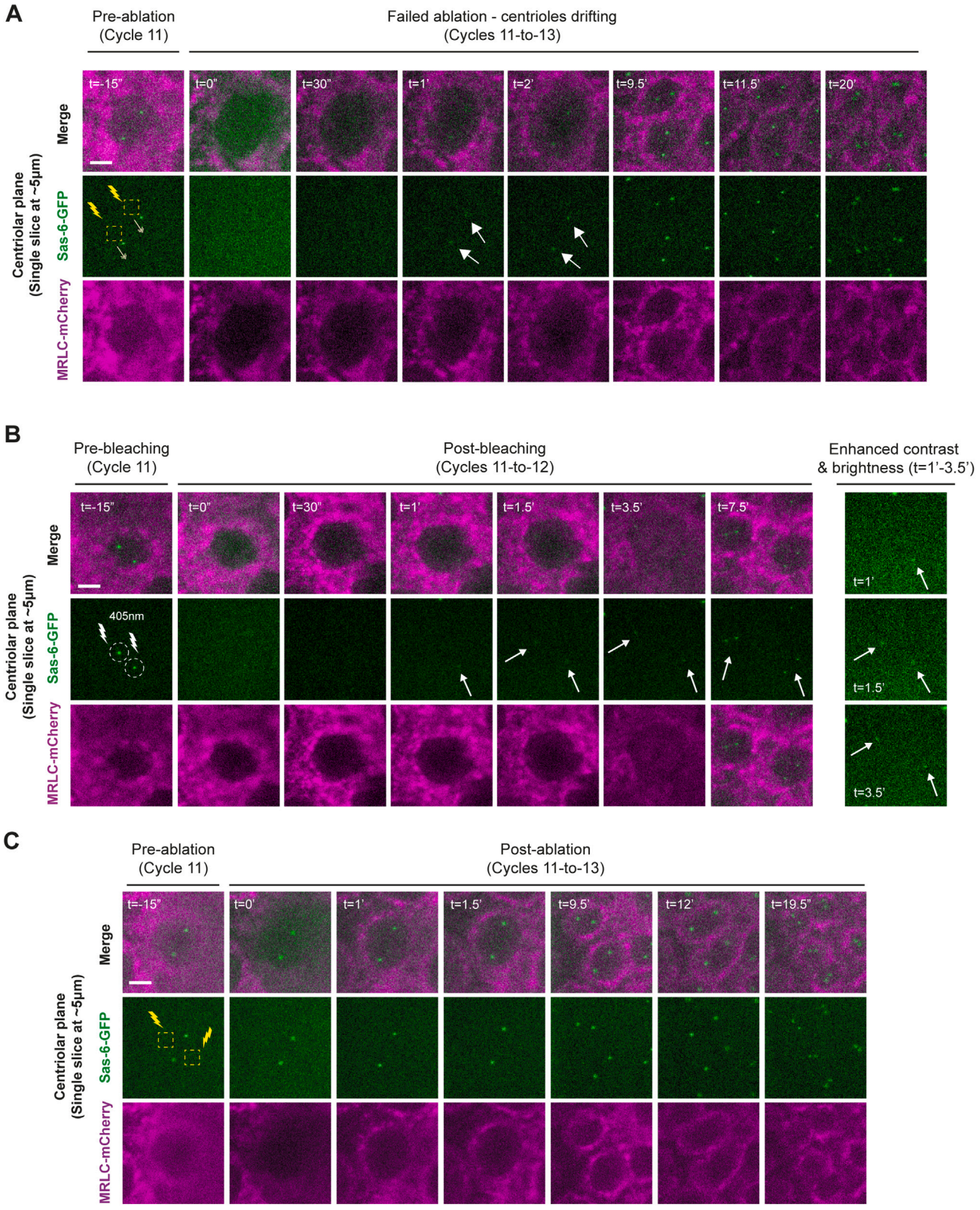

(legend on next page)

Figure S5. Controls for the laser ablation experiments, related to Figure 4

(A) Micrographs depict compartments (MRLC-mCherry) where we intended to ablate the centrioles (Sas-6-GFP) in early interphase (middle). Due to the embryonic flows, the centrioles progressively moved out of the target region (dashed yellow squares) during the ablation process (arrows with double-heads indicate the movement of the centrioles in the southeast direction away from the region of ablation). As such, the centriolar Sas-6-GFP was inadvertently bleached, instead of being ablated. The signal recovers within ~1 min (as pointed by the white arrows in t = 1′–2′) and becomes more robust as time progresses.

(B) Images demonstrate our control experiment for the interpretation of (A), where instead of ablating the centrioles, we intentionally bleached their signal with a 405 nm laser (dashed white circles). Like in (A), the signal here also recovered within 1′–2′ (indicated by white arrows), and even more robustly in the next cell cycle (t = 7.5′). Panels on the right (Sas-6-GFP only) are the same as the time series 1′–3.5′ on the left, except for their enhanced brightness and contrast to better highlight the signal recovery.

(C) Micrographs demonstrate another control experiment to see whether ablating a pair of regions neighboring where the centrioles are (but not on them) would bleach/ablate the centrioles as well. We did not find this to be the case, and this perturbation did not lead to any other, adverse effect on the cell cycle either. Panels in (A)–(C) are all representative of n = 3 independent experiments in each scenario. Scale bars, 5 μm.

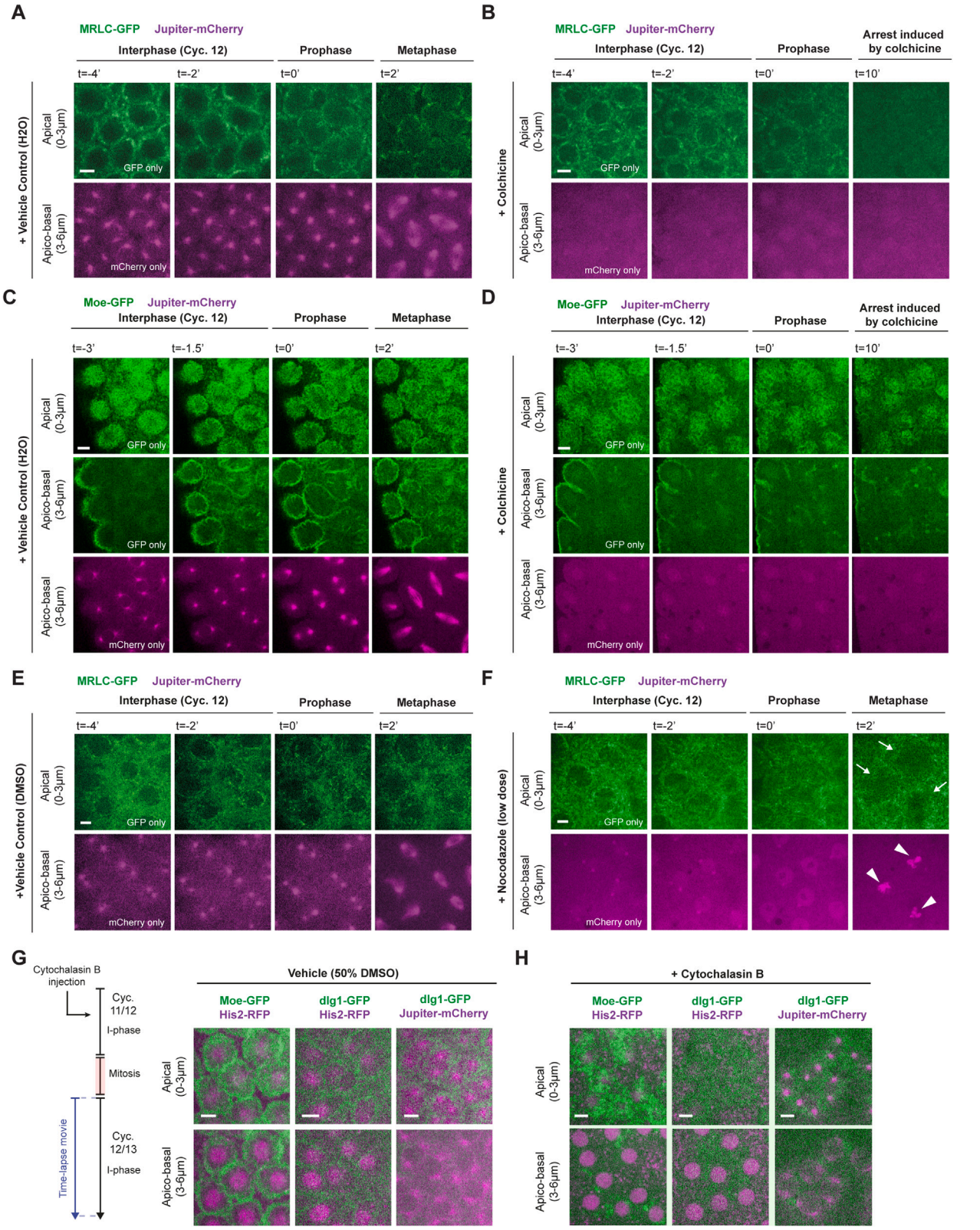

(legend on next page)

Figure S6. Time-lapse snapshots of MT and actin filament depolymerization experiments, related to Figures 5 and 7

(A and B) Time-lapse images depict cytoplasmic compartments (MRLC-GFP) and microtubules (Jupiter-mCherry) in embryos injected either with (A) the drug vehicle (H_2O; n = 5) or (B) colchicine (n = 5).

(C and D) Same as in (A) and (B) but in embryos expressing Moe-GFP and Jupiter-mCherry (n = 5 embryos per group).

(E and F) Time-lapse images depict cytoplasmic compartments and microtubules in embryos injected either with (E) the drug vehicle (DMSO; n = 3) or (F) nocodazole (n = 5). Although colchicine injection leads to gradual destruction of cytoplasmic compartments (B and D), nocodazole injection (at ~15 ng/mL effective concentration, impairing centrosomal but not chromatin-mediated MT polymerization) enables re-organization of cytoplasmic compartments (F), albeit less robustly (n = 4 embryos). See in (F) how the beginning of chromatin-mediated MT polymerization coincides with when the cytoplasmic compartments reorganize (indicated by white arrows). Representative images from the time series from (A)–(F) were used to make the main points in Figure 5A.

(G and H) Micrographs illustrate the state of cytoplasmic compartments (G) in embryos injected with a drug vehicle (DMSO; n = 5 per group), expressing a variety of genetic markers in combination, or (H) in embryos injected with cytochalasin B (n = 5 per group). Note in (H) how the nuclear divisions can continue in the absence of cytoplasmic compartments (bottom set of panels), albeit with a number of nuclear defects (see Figure S7A and Video S6). The scheme next to the panels illustrates the injection protocol. Scale bars, 5 μm.

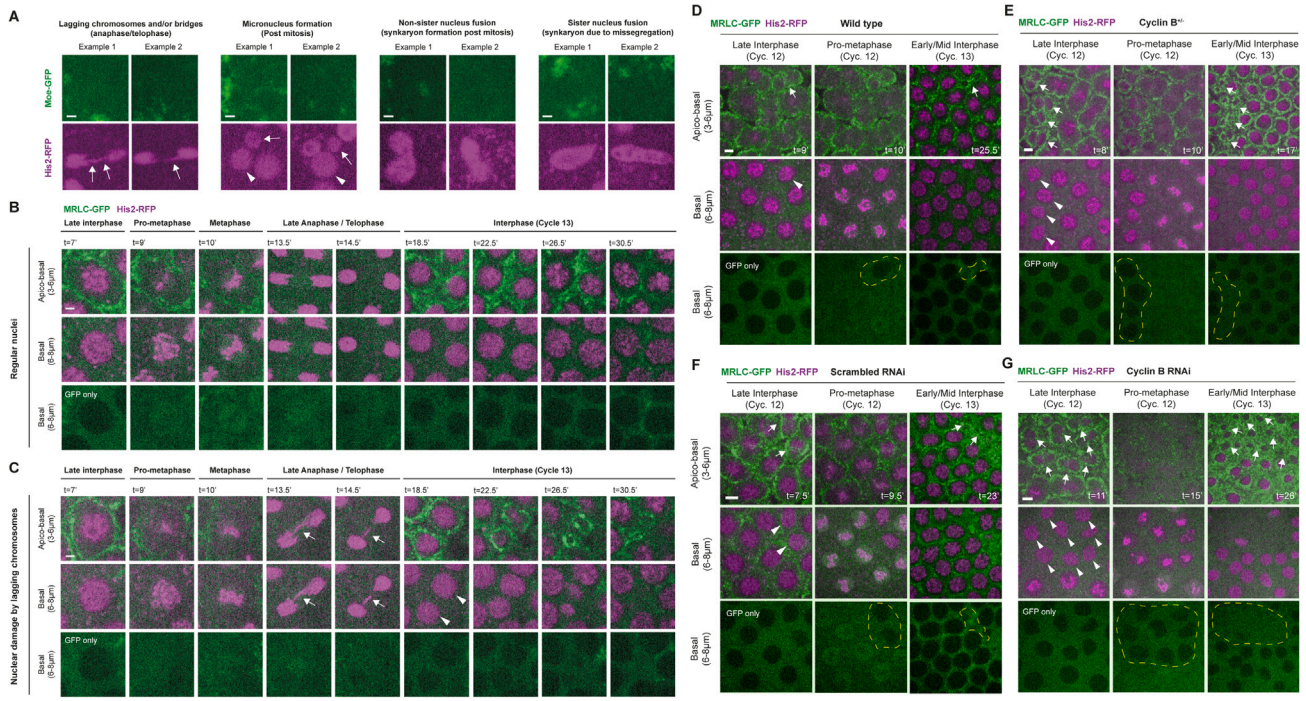

Figure S7. Like the well-known elimination of nuclei with karyotype damages, the mitotically delayed nuclei are also eliminated—likely via an extrusion-based mechanism by autonomous cytoplasmic divisions, related to Figure 7

(A) In pairs of example nuclei, micrographs illustrate four different types of nuclear damages that arise upon the collapse of cytoplasmic compartments in embryos injected with cytochalasin B (judged by the loss of compartment organization in the Moe-GFP channel). White arrows in the first panel point out the lagging chromosomes, whereas the ones in the second panel indicate the micronuclei that stem from their "mother" nuclei (marked by white arrowheads). Scale bars, 2 μm.

(B and C) Time-lapse micrographs show the fate of nuclei from interphase (cyc.12) to interphase (cyc. 13) in embryos expressing MRLC-GFP and His2-RFP. Basal GFP-only channels help visualizing the nuclear entry into, and exit from, mitosis.

(B) Under normal circumstances, nuclei go through mitosis and continue to reside apically in the blastoderm.

(C) As demonstrated by previous studies,[62–64] nuclei with karyotype damages (e.g., lagging chromosomes that form anaphase bridges as indicated by white arrows) are usually eliminated from the blastoderm by fallout (follow white arrowheads). In our experiments, we can observe both nuclear extrusions (Figures 7A and 7B; type 1) and fallouts (depicted here; type 2) within the same embryos (see Video S4). Scale bars, 2 μm.

(D–G) Micrographs illustrate the state of mitotically delayed nuclei (interphase to next interphase) in (D) unperturbed WT (n = 9) and (E) CycB$^{+/-}$ embryos (n = 9), or in embryos (F) injected with dsRNA against a scrambled sequence (n = 8), or (G) with dsRNA against cyclin B (n = 7). In all conditions, the embryos express MRLC-GFP and His2-RFP simultaneously. White arrows (top) highlight the cytoplasmic compartments that divide independently of the mitotically delayed nuclei associated with them (indicated by white arrowheads in the basal panel). Mitotically delayed nuclei and their extrusions are highlighted by yellow dashed lines. See the noticeable increase in the delays and extrusions in (E) and (G) in comparison with control embryos in (D) and (F), respectively (quantifications and the sample size for each group are reported throughout Figure 7). Scale bars, 5 μm.